Coordination Chemistry Reviews 556 (2026) 217718

Contents lists available at ScienceDirect

Coordination Chemistry Reviews

journal homepage: www.elsevier.com/locate/ccr

Recent advances in size-specific spectroscopy of metal carbonyl complexes

Hua Xie [a,*], Gang Li [a], Ling Jiang [a,b,*]

[a] State Key Laboratory of Chemical Reaction Dynamics and Dalian Coherent Light Source, Dalian Institute of Chemical Physics, Chinese Academy of Sciences, Dalian 116023, China
[b] Hefei National Laboratory, Hefei 230088, China

ARTICLE INFO

Keywords:
Metal carbonyls
Infrared–vacuum ultraviolet spectroscopy
Photoelectron spectroscopy
Quantum chemical calculations

ABSTRACT

Metal carbonyl complexes provide unique platforms for probing metal–ligand bonding, electronic structures, and catalytic mechanisms. This review focusses on recent advances in a series of novel homometallic and heterobimetallic carbonyl complexes studied by infrared–vacuum ultraviolet spectroscopy, photoelectron spectroscopy, and quantum chemical calculations. This combined approach enables accurate determination of vibrational characteristics, electron detachment energies, and bonding motifs, allowing clear differentiation between σ-donation, π-back-donation, and metal–metal interactions. Investigations of group-3 homoleptic carbonyls identified the first neutral confinement-free species: $Sc(CO)_7$ and $M(CO)_8$ (M = Y, La). Spectroscopic observation of neutral $OTiCCO(CO)_n$ (n = 2–5) served as the fresh evidence for efficient C—O cleavages and concomitant C—C formations. Studies of heterobimetallic carbonyl complexes $MFe(CO)_4^-$ (M = Ti, *V*, Cr, Si, Ge, Sn) and $MNi(CO)_n^-$ (M = Sc, Y, Ti, Zr, Hf, V; n = 3–5) indicated coordination preferences dictated by both cluster size and metal identity, along with associated charge redistribution and CO-activation pathways, all of which bear direct relevance to surface catalysis. Collectively, these studies established the well-defined clusters as functional molecular analogues of catalytically active sites, effectively bridging fundamental bonding concepts with applications in CO/CO_2 utilization, syngas chemistry, and energy-conversion processes.

1. Introduction

Metal carbonyl complexes have constituted a foundational framework for the development of inorganic and physical chemistry since their discovery in the late 19th century [1–3]. As the first well-defined metal–ligand coordination compounds [4,5], metal carbonyl complexes have served as indispensable model systems for developing foundational concepts such as electron-counting schemes, the 18-electron rule [6,7], the ligand field theory [8,9], and the bonding model of Dewar–Chatt–Duncanson [10–12]. Unique electronic characters of carbon monoxide (CO) [13–15], which act as both a strong σ-donor via its 5σ orbital and as an excellent π-acceptor through its 2π* orbital, makes metal carbonyl complexes ideal platforms for examining the intricate interplay between donation and back-donation in coordination bonding [16–20]. Beyond their pedagogical importance, metal carbonyls are essential in catalysis and energy science [21–24]. They serve as molecular analogues for CO adsorption and activation on heterogeneous catalytic surfaces [25,26], processes central to industrially important reactions such as Fischer–Tropsch synthesis, hydroformylation, syngas conversion, and enzymatic CO/CO_2 fixation [27–38]. In addition, their structural diversity, spanning simple mononuclear carbonyls to complex polynuclear clusters, enables detailed investigations of metal–metal interactions and ligand dynamics [39–46]. Therefore, it is essential to decipher the geometric structures, electronic properties and reactive behaviors of metal carbonyl complexes in order to advance fundamental coordination chemistry, inform the rational design of catalysts and develop strategies for the sustainable utilization of carbon resources.

Scheme 1 shows a brief timeline of the development of metal carbonyl complexes. Over the past decade, major advances have been made in both spectroscopic techniques [47–62] and computational frameworks [63–72] for probing metal carbonyl clusters. Experimentally, photoelectron spectroscopy (PES) has become a significant tool to determine electron detachment energies, spin states, and electronic configurations of mass-selected ionic species [73–84]. Vibrational methods (i.e., infrared photodissociation (IRPD) spectroscopy [85–93] and infrared–vacuum ultraviolet (IR–VUV) double-resonance spectroscopy [94–102]) allow accurate measurement of CO stretching frequencies, enabling unambiguous identification of coordination motifs such as bridging, terminal, and side-on-bonded modes. These high-

* Corresponding authors.
E-mail addresses: xiehua@dicp.ac.cn (H. Xie), ljiang@dicp.ac.cn (L. Jiang).

https://doi.org/10.1016/j.ccr.2026.217718
Received 7 January 2026; Accepted 9 February 2026
Available online 13 February 2026

resolution gas-phase techniques provide essential benchmarks for validating theoretical models and for assigning isomeric structures that are challenging to resolve in condensed phases. On the theoretical front, the adoption of dispersion-corrected density functional theory (DFT) (e.g., B2PLYP-D3, PBE—D3) and double-hybrid functionals [103,104], together with relativistic treatments like the zero-order regular approximation (ZORA), has considerably improved the predictive accuracy of geometric parameters and energetics, especially for clusters containing heavier metals [105–107]. At the same time, energy decomposition analysis in conjunction with natural orbitals for chemical valence (EDA-NOCV) has become an essential tool for quantifying the respective bonding contributions in metal carbonyls [108]. These advances in experimental and computational methodologies have established a tightly integrated platform for the comprehensive characterization of reactive, electronic, and structural properties of metal carbonyl complexes.

In this context, both homometallic and heterobimetallic carbonyl complexes have revealed a wealth of bonding motifs and reactivity patterns. The systems summarized in this work include neutral group-3 homoleptic carbonyls, $OTiCCO(CO)_n$ (n = 2–5), $MFe(CO)_4^-$ (M = Ti, *V*, Cr, Si, Ge, Sn), and $MNi(CO)_n^-$ (M = Sc, Y, Ti, Zr, Hf, V; n = 3–5), which demonstrate how metal identity and ligand coordination govern structural preferences, thermodynamic stability, and spectroscopic signatures [109–115]. These representative cases highlight the value of size-selected metal carbonyl complexes as model platforms for elucidating fundamental metal–ligand interactions. Beyond these systems, numerous classical carbonyl complexes also broadened and deepened our understanding [59,116–129]. Dimers such as $Co_2(CO)_8$ and $Mn_2(CO)_{10}$ represent archetypal systems featuring metal–metal bonding mediated by bridging carbonyl ligands [118], while trinuclear clusters including $Fe_3(CO)_{12}$, and $Os_3(CO)_{12}$ demonstrate how electron delocalization in triangular metal frameworks imparts distinctive stability and reactivity [121]. Mononuclear hexacarbonyls such as $W(CO)_6$ and $Mo(CO)_6$ serve as benchmark octahedral complexes, highlighting group-dependent trends in orbital overlap, vibrational signatures, and photochemical behavior [125]. In bioinorganic chemistry, Ni—Fe and Fe—Fe carbonyl complexes serve as structural and functional mimics of hydrogenase active sites, where CO ligation plays a key role in modulating enzymatic activity [130–132].

This review summarizes recent advances in metal carbonyl chemistry, with particular emphasis on homometallic and heterobimetallic carbonyl complexes. The present systems encompass a wide range of bonding architectures, ranging from conventional terminal and bridging CO coordination to non-canonical motifs such as OTiCCO-based isomers that challenge classical bonding paradigms [110]. A key strength of this body of work lies in its integrated methodological approaches: IR–VUV spectroscopy enables isomer-specific vibrational characterization of neutral metal carbonyl complexes, PES provides direct information of electronic structures, detachment energies of anionic complexes, and advanced DFT calculations provide reliable structural assignments and bonding analyses. Beyond advancing fundamental mechanistic understanding, these findings offer molecular-scale analogues of heterogeneous catalytic interfaces, bridging the gap between bonding theory and applied catalysis. By contextualizing these results in the broader context of metal carbonyl chemistry, this review underscores their value as benchmarks for theoretical validation, as structural and functional models of catalytically active sites, and as innovative platforms for the development of sustainable strategies in carbon science, syngas processing, and energy-relevant transformations [133].

2. Methodological advances in metal carbonyl studies

2.1. Experimental methods

2.1.1. Infrared–vacuum ultraviolet (IR–VUV) spectroscopy

The experimental configuration for IR–VUV methods has been thoroughly documented in previous works [134]. Briefly, $Sc(CO)_7$ and $M(CO)_8$ neutral complexes (M = Y, La) were produced using laser vaporization of 100% CO in a supersonic expansion. Neutral Ti carbonyl complexes were obtained in 10% CO/He via a pulse valve of Even–Lavie (EL-7-2011-HT-HRR). An Nd:YAG laser operating at its second harmonic (532 nm) was used to vaporize the Sc, Y, La and Ti metals, with a backing pressure of approximately 50 atm. The metal products were successively collimated by a skimmer. Charged species were then deflected and entered into a mass spectrometry system. Size-selected Sc $(CO)_7$, $M(CO)_8$ (M = Y, La), and $OTiCCO(CO)_n$ (n = 2–5) complexes were probed by carefully optimizing the experimental conditions.

Resonant IR photon absorption induced vibrational pre-excitation of the complexes, thereby enhancing ionization efficiency for species with ionization potentials marginally exceeding the VUV photon energy. Size-selected neutral complexes were spectroscopically characterized by recording IR wavelength-dependent signal enhancement in the mass-resolved ion yield. Infrared spectra were derived from its relative enhancement of ion signals under IR irradiation, $I(\nu)/I_0$, converted into

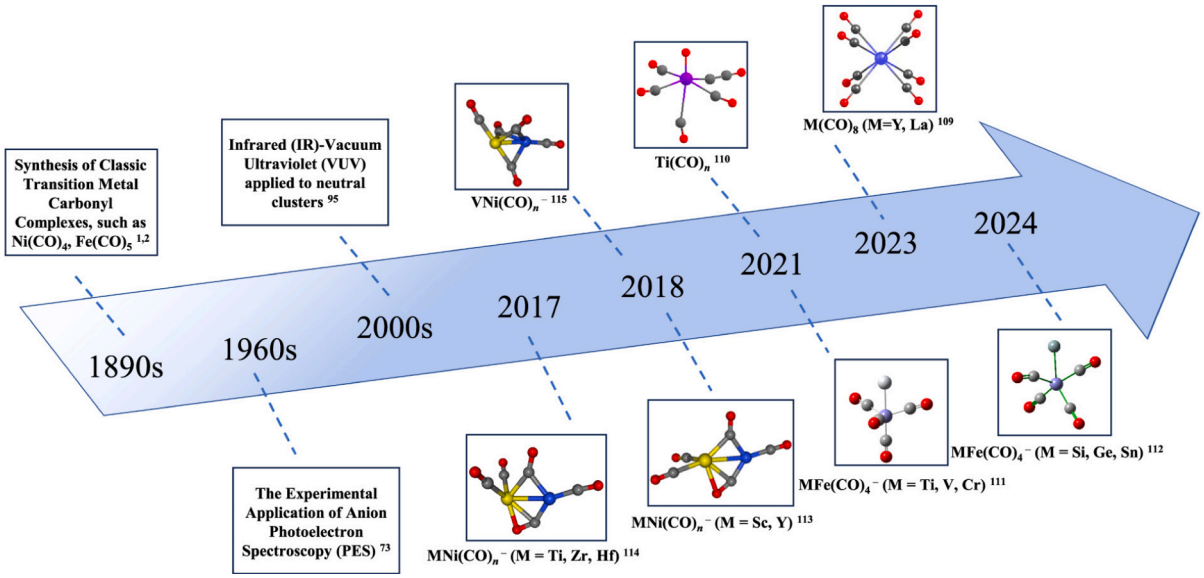

Scheme 1. Timeline of important milestones in the development of metal carbonyl complexes.

relative absorption cross sections $\sigma(\nu)$ via the relation $\sigma(\nu) = -\ln[I(\nu)/I_0]/P(\nu)$. Normalization by the infrared laser energy $P(\nu)$ corrected for fluctuations in pulse energy across its tuning range. The spectra were generally acquired using scanning the infrared laser in 2 cm^{-1} increments. The IR spectra of $Sc(CO)_7$ and $M(CO)_8$ (M = Y, La) complexes were measured at 193.00 nm. The IR spectra of neutral $OTiCCO(CO)_n$ (n = 2–5) species were recorded at 140.00 nm for $n = 2$ and 3, at 153.00 nm for $n = 4$, and at 158.50 nm for $n = 5$. Insufficient particle densities for species with $n \leq 1$ and $n \geq 6$ precluded acquisitions of well-resolved spectra. Consequently, spectral characterization of individual VUV pulses was performed via an on-line vacuum ultraviolet spectrometer to ensure pulse-to-pulse spectral fidelity.

2.1.2. Photoelectron spectroscopy (PES)

Experimental PES measurements were detailed elsewhere [135]; the present work offers a concise summary of its principal features. The target heterobinuclear carbonyls, including $MFe(CO)_4^-$ (M = Ti, *V*, Cr, Si, Ge, Sn) and $MNi(CO)_n^-$ (M = Sc, Y, Ti, Zr, Hf, V; n = 3–5) were synthesized in a supersonic cluster source based on laser vaporization. The nascent metal clusters, produced via laser ablation, were entrained in a helium carrier gas containing 5% CO at pressures of 1–5 atm, promoting efficient carbonyl coordination and stabilization of the resulting complexes. The ensuing beam of anions underwent skimming within a differentially pumped region before a mass spectrometer of the McLaren–Wiley design [136]. The mass-selected anions were then directed into its photodetachment interaction region and irradiated with photon beams at either 355 nm (3.496 eV) or 266 nm (4.661 eV), produced by an Nd:YAG laser system. Photoelectrons ejected from the anions were velocity-mapped onto a two-dimensional detection assembly comprising a phosphor screen with a microchannel plate. The experimental images were revealed with a CCD camera, with 10,000–50,000 pulse laser shots from each accumulated image. Reconstruction of the experimental images was performed using the Basis Set Expansion inverse Abel transform algorithm [137], as detailed in the following sections. The photoelectron spectra were calibrated using the reference-standard Au^- photoelectron spectrum, yielding an energy kinetic energy resolution better than 5%. This corresponds to an absolute resolution of approximately 50 meV at 1 eV [82]. The experimental vertical detachment energy (VDE) was directly measured from the band maximum of PES spectrum. The experimental adiabatic detachment energy (ADE) was derived by extending a line from the leading edge of the VDE peak and adding the instrumental resolution at the point where the line intersects with the horizontal axis. The experimental VDE and ADE error bars were determined by the energy resolution at the corresponding electron kinetic energy.

2.2. Theoretical methods

Theoretical computations were fulfilled by Gaussian 09 software package [138]. The possible electronic states of anionic and neutral structures have been calculated. The VDE was computed by the difference in energy between the neutral and anionic species at the optimized geometry of the anion. The ADE was determined as the difference in energy between the fully optimized structures of the anionic and the neutral cluster. Zero-point energy corrections were included in ADEs and relative energies. Additional electronic structure analyses were applied by using the Multiwfn soft [139], including evaluation of unpaired spin density distributions through isosurface mapping, calculation of electrostatic potential surfaces, natural atomic orbital population analyses, and Wiberg bond orders [140,141]. Visualization of spin density isosurfaces and electrostatic potential maps was further enhanced by using the Visual Molecular Dynamics software [142]. To elucidate the bonding nature of the metal–CO interactions, EDA-NOCV analyses were performed and complemented by wavefunction-based methods [108]. Relative electronic energies and reaction barriers were obtained for structures optimized at 0 K, and zero-point vibrational energy corrections were included.

3. Results and analysis

3.1. $M(CO)_n$ (M = Sc, Y, La; n = 7, 8)

3.1.1. Experimental infrared spectra

The IR–VUV spectroscopy approach enabled the generation and characterization of neutral carbonyl complexes $M(CO)_n$ (M = Sc, Y, La). The complete experimental procedure was described in the Experimental Section [134]. Fig. 1 presents experimental and simulated IR spectra in the ν(CO) region (1900–2100 cm^{-1}) alongside DFT-optimized equilibrium geometries for $Sc(CO)_7$ and $M(CO)_8$ (M = Y, La) [109]. The experimental result of $Sc(CO)_7$ displays a prominent peak at 1970 cm^{-1}, and it has distinct shoulders at 1978/1992 cm^{-1}, along with a weaker feature of 2082 cm^{-1}. In contrast, $Y(CO)_8$ and $La(CO)_8$ exhibit a single peak, symmetric peak at 2000 and 2010 cm^{-1}. All complexes exhibit considerable red-shift phenomenon in C—O stretching frequencies (free CO: 2143 cm^{-1}). This frequency lowering is attributed to back-donation from metal d orbitals into the antibonding $2\pi^*$ orbitals of CO, a key bonding interaction often termed π back-donation. The red shift follows the trend Sc < Y < La, indicating decreasing back-donation strength across the group 3 metals. This trend arises from the progressive radial expansion of d-orbitals and the increasing effective nuclear charge, which collectively influence orbital overlap and the π-back/σ donation balance [109].

Furthermore, the presence of a single IR-active C—O band in the spectra of $Y(CO)_8$ and $La(CO)_8$ indicates highly symmetric molecular structures. These findings are consistent with octacarbonyl complexes adopting nearly ideal O_h or D_{4h} symmetry, in which all carbonyl ligands are equivalent from a spectroscopic perspective. In contrast, the multiple bands observed in the $Sc(CO)_7$ spectrum suggest a lower-symmetry structure, likely reflecting inequivalent CO binding sites. The weak, high-frequency peak of 2082 cm^{-1} is probably related to a terminal CO ligand that experiences minimal back-donation, as indicated by its closeness to the stretching frequency of free CO [109].

3.1.2. Comparison between experimental and theoretical results

DFT theory calculations of the PBE functional [143] were applied to obtain equilibrium geometries and harmonic vibrational frequencies of the complexes $M(CO)_n$ (M = Sc, Y, La). All calculations were executed by the ADF 2021 software suite [144]. Explicit consideration of scalar relativistic effects was achieved via the ZORA formalism [105–107]. Two additional polarization functions (TZ2P) with the basis sets of triple-ζ quality Slater-type orbital were employed for all atoms to guarantee balanced precision [145]. The frozen-core approximation was applied to the [$1s^2$] shell of C and O, the [$1s^2$–$2p^6$] shells of Sc, the [$1s^2$–$3d^{10}$] shells of Y, and the [$1s^2$–$5p^6$] shells of La [146].

The experimental carbonyl stretching frequency of free CO is 2143 cm^{-1}, and the calculated value is 2124 cm^{-1}. By the ratio of the experimental and calculated results, we can obtain a scaling factor of the calculated harmonic vibrational frequencies is 1.009. This scaling improves the accuracy of comparisons between theoretical and experimental spectroscopic data. For $Sc(CO)_7$, the simulated spectrum features a single band centered at 1985 cm^{-1}, which is from two nearly degenerate vibrational modes of 1984 cm^{-1}. This shows good agreement with the experimental spectrum, which exhibits an absorption band at 1970 cm^{-1}. Similarly, the nearly degenerate modes calculated at 1994/1999 cm^{-1} combine into a single peak at 1994 cm^{-1}, matching the experimental shoulder at 1978 cm^{-1}. Additionally, two weaker calculated bands at 2022/2091 cm^{-1} correspond to the experimental absorptions at 1992/2082 cm^{-1}. These agreements indicate that the theoretical spectrum accurately reproduces both the dominant and minor spectral features of $Sc(CO)_7$. The simulated spectrum of $Y(CO)_8$ predicts three C—O stretching vibrations with almost nearly degenerate that merge to yield a single, intense absorption peak at 2001 cm^{-1}, which is in

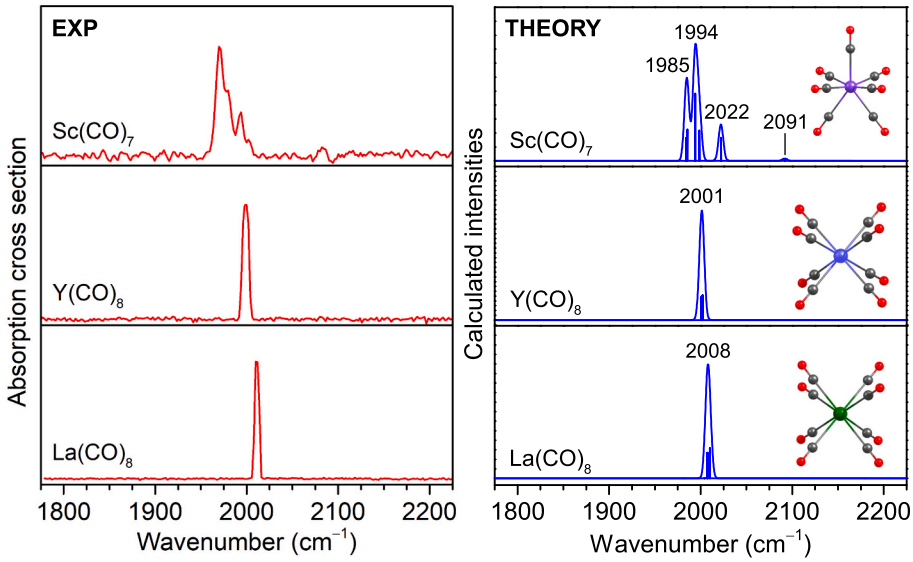

Fig. 1. Experimental and simulated IR spectra and optimized equilibrium geometries of neutral $Sc(CO)_7$, $Y(CO)_8$, and $La(CO)_8$ carbonyl complexes. Reproduced with permission [109].

excellent accord with 2000 cm^{-1}. A comparable level of accord is found for $La(CO)_8$, where the calculated spectrum produces a single prominent feature that closely matches the experimental absorption at 2010 cm^{-1} [109].

The remarkable congruence between scaled DFT-computed frequencies and experimental IR absorption bands provides unequivocal validation for the structural assignments of the global-minimum isomers of the current three neutral species. The computational models successfully reproduce both the fine spectral features of the lower-symmetry Sc complex and the single-band patterns characteristic of the highly symmetric Y and La octacarbonyls, further confirming the reliability of the computational approach used.

3.2. $OTiCCO(CO)_n$ ($n = 2$–5)

3.2.1. Experimental infrared spectra

Neutral titanium carbonyls were generated and subsequent analysis was performed by IR-VUV methods [134]. Mass spectra of these $OTiCCO(CO)_n^+$ cations obtained from the ionization at different VUV-FEL wavelengths are found in Fig. 2, and the experimental and simulated infrared spectra were indicated in carbonyl-stretching region for $OTiCCO(CO)_n$ ($n = 2$–5) complexes in Fig. 3 [110].

All detected complexes show two more distinct absorption bands above 2070 cm^{-1}, with wavenumbers spanning 2071 to 2167 cm^{-1} [110]. The measured frequencies of $Ti(CO)_n$ ($n = 4$–7) were significantly reported about 1800–1991 cm^{-1} [147]. This pronounced blue-shift indicates that the gas-phase species adopt distinct structural motifs in which the Ti center exhibits a more pronounced electropositive character compared with their matrix-isolated counterparts. This effect is attributed to reduced metal–CO back-donation under gas-phase conditions, which lowers the electron occupancy in the CO π* orbitals, thereby increasing the C—O bond order is elevated with an increase in the observed vibrational frequencies. Furthermore, for every gas-phase complex, the band at the lowest energy is situated just above the reported carbonyl stretching frequency reported for the previously characterized OTiCCO molecule, which is 2047.7 cm^{-1} in an argon matrix [148]. This consistent spectral alignment suggests that the gas-phase species are more likely structural isomers of $OTiCCO(CO)_n$ rather than conventional homoleptic carbonyl complexes. These results highlight the considerable influence of coordination environment and oxidation state on the vibrational properties of metal carbonyl species, and demonstrate the effectiveness of gas-phase spectroscopy for identifying reactive intermediates that are difficult to study in condensed phases.

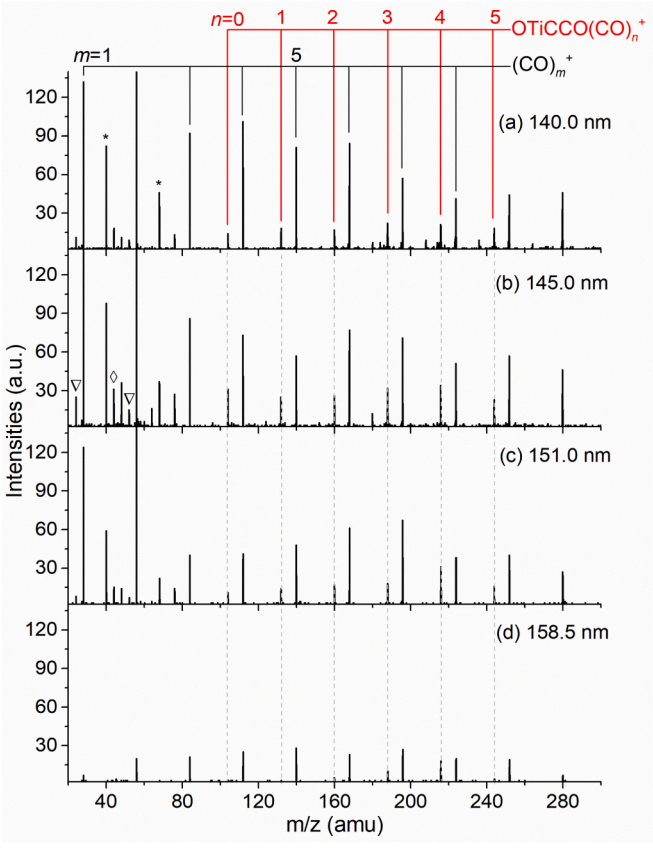

Fig. 2. Time-of-flight mass spectra of the $OTiCCO(CO)_n^+$ cations produced from the ionization at different VUV-FEL wavelengths. Reproduced with permission [110].

3.2.2. Comparison between experimental and theoretical results

Theoretical calculations for $OTiCCO(CO)_n$ ($n = 2$–5) complexes were executed with the Gaussian 09 suite [138]. Initial geometry optimizations were performed at the B2PLYP-D3/def2-TZVPP level of theory to

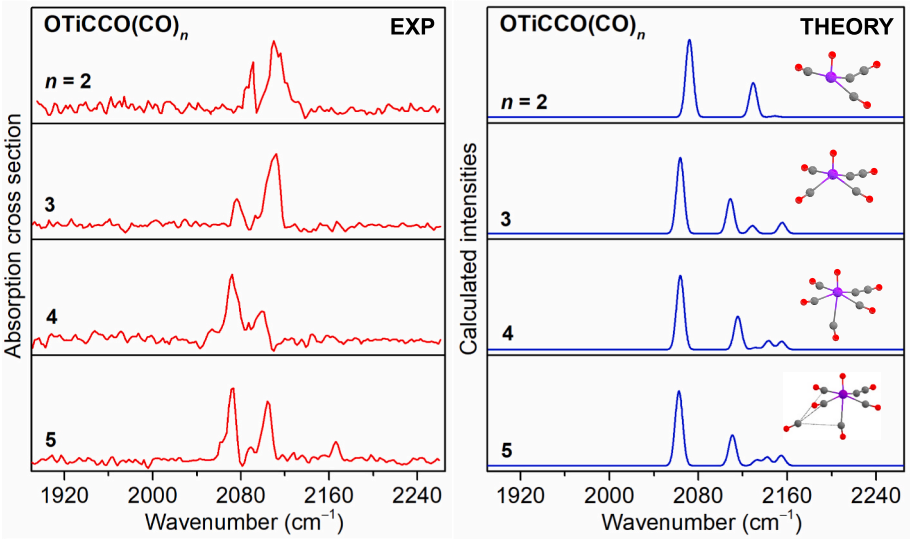

Fig. 3. Experimental and simulated IR spectra and optimized equilibrium geometries of neutral OTiCCO(CO)$_n$ (n = 2–5) complexes. Reproduced with permission [110].

account for dispersion interactions and provide reliable structural parameters [149]. Relative electronic energies and reaction barriers were computed at the optimized 0 K geometries. Harmonic frequencies were calculated and scaled by a factor of 0.991 to mitigate systematic

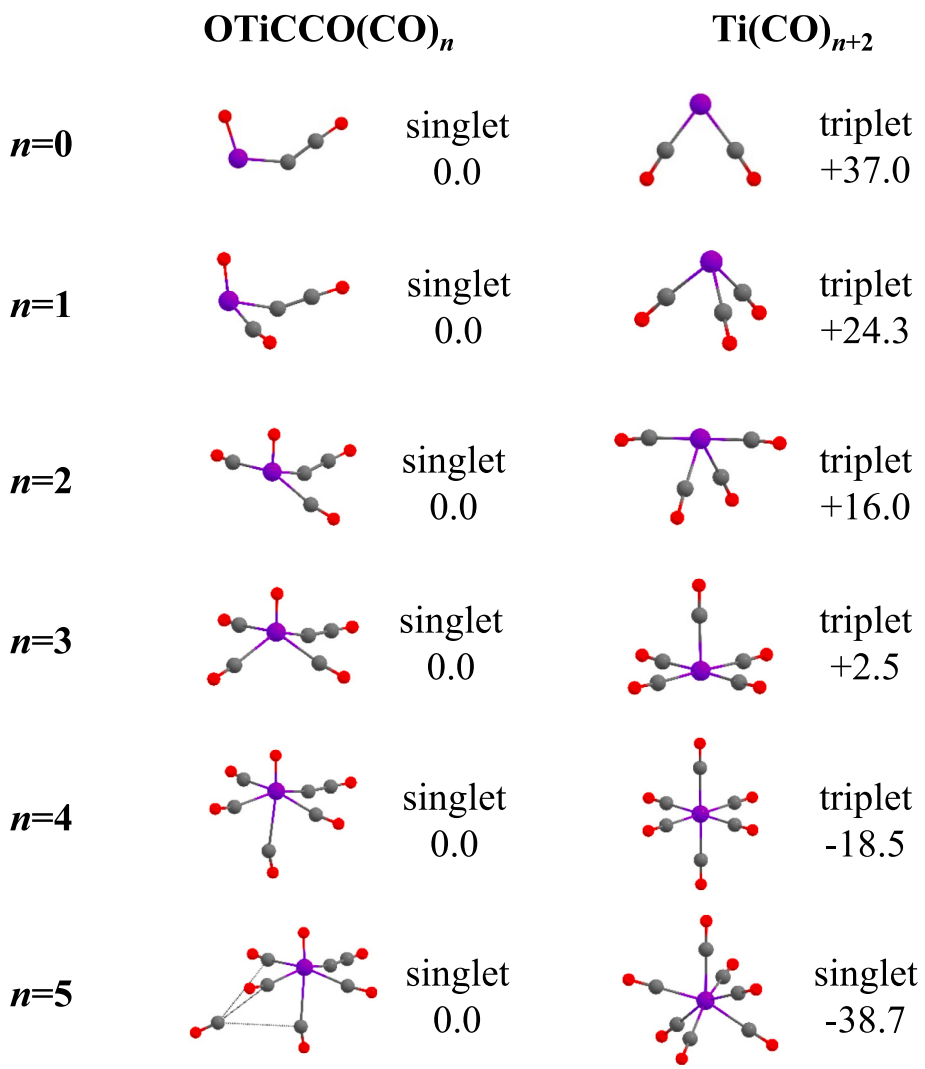

Fig. 4. Optimized structures and relative energies (kcal/mol) of neutral OTiCCO(CO)$_n$ and Ti(CO)$_{n+2}$ (n = 0–5) clusters. Reproduced with permission [110].

overestimation typical for this method. The theoretical IR stick spectra were generated and subsequently broadened using a Gaussian function with a full width at half maximum (FWHM) of 8 cm^{-1}, enabling direct comparison with the experimental IR spectra.

For each complex, two distinct structural types were identified in Fig. 4. One contains an OTiCCO core, formulated as $OTiCCO(CO)_n$; the other is the conventional homoleptic titanium carbonyl $Ti(CO)_{n+2}$. A close match to its IR experimental spectrum is provided by the simulation of the $OTiCCO(CO)_5$ isomer, supporting the observation of $n = 5$ species. This structural identification is particularly important because $OTiCCO(CO)_5$ is computationally 38.7 kcal·mol^{-1}, which is less stable than the homoleptic $Ti(CO)_7$ isomer. The energetic preference for $Ti(CO)_7$ highlights the important role of kinetic and spectroscopic factors in determining which species are observed under experimental conditions [110]. Consistent support for the $OTiCCO(CO)_n$ structural assignment over the conventional $Ti(CO)_{n+2}$ isomer is provided by a thorough spectral comparison for the $n = 2$–4 complexes [110].

3.3. $MFe(CO)_4^-$ (M = Ti, V, Cr, Si, Ge, Sn)

3.3.1. Photoelectron spectra

The experimental observed photoelectron results of $MFe(CO)_4^-$ anions (M = Ti, V, Cr) were measured at a photon wavelength of 266 nm (Fig. 5), alongside the spectra of $MFe(CO)_4^-$ (M = Si, Ge, Sn) recorded at 355 nm [111,112]. In all cases, the first spectral features correspond to ground-state electronic transitions of the respective anions. Notably, the spectra for $MFe(CO)_4^-$ with M = Ti, V, Cr display broadly featureless profiles. This spectral broadening is likely attributed to the population of vibrationally and electronically excited states in the anions, which are generated under the high-temperature conditions. In addition to the effects of the hot cluster source, other factors may also contribute to the observed spectral broadening. Factors contributing to this broadening include considerable geometric reorganization following photodetachment, the possible coexistence of multiple energetically degenerate isomers, and the presence of densely spaced stable electronic states. Notably, the spectrum of $TiFe(CO)_4^-$ is considerably broader than those of $VFe(CO)_4^-$ and $CrFe(CO)_4^-$, which may reflect either the presence of multiple isomeric forms or substantial structural rearrangements upon electron detachment.

Furthermore, the spectrum of $SiFe(CO)_4^-$ shows additional broadening at higher electron binding energies (eBEs), suggesting the possible involvement of a two-photon detachment process or contributions from excited electronic states. The *V*DEs of these $MFe(CO)_4^-$ series, determined from the respective band maxima, are 2.49 ± 0.11, 2.75 ± 0.10, 2.97 ± 0.08, 2.06 ± 0.07, 1.96 ± 0.08, and 1.88 ± 0.08 eV, while the corresponding ADEs are 2.20 ± 0.12, 2.32 ± 0.12, 2.58 ± 0.10, 2.06 ± 0.07, 1.96 ± 0.08, and 1.88 ± 0.08 eV [111,112].

3.3.2. Comparison between experimental and theoretical results

Geometry optimizations and electronic structure analyses of $MFe(CO)_4^-$ (M = Ti, V, Cr) were conducted using the BP86 generalized gradient approximation (GGA) functional. In contrast, calculations for the main-group series (M = Si, Ge, Sn) employed the B3LYP hybrid functional. Within the transition metal set, carbon and oxygen atoms have been calculated with the 6–311 + G(d) basis set [150], while the SDD basis set was utilized for the metal centers [151]. For the group 14 analogues, a consistent theoretical treatment was achieved by applying the all-electron def2-TZ*V*PP to all atoms in these systems [149]. The globally optimized, lowest-energy geometries determined for all $MFe(CO)_4^-$ anions (M = Ti, V, Cr, Si, Ge, Sn) are indicated in Fig. 6 [111,112].

For $MFe(CO)_4^-$ (M = Ti, V, Cr), the global minimum-energy structures (denoted 4 A, 4B, and 4C, respectively) adopt trigonal–bipyramidal geometries with C_{3v} symmetry, in which the heterometal atom M occupies an axial position coordinated to the iron center [152–154]. Electronic structure calculations reveal high-spin ground states for the $MFe(CO)_4^-$ anions: a quartet state ($^4A_1$) for $TiFe(CO)_4^-$, a quintet state ($^5A_1$) for $VFe(CO)_4^-$, and a sextet state ($^6A_1$) for $CrFe(CO)_4^-$ [111]. Conversely, the lowest-energy isomers of the group 14 anions $MFe(CO)_4^-$ (M = Si, Ge, Sn) (designated 4a, 4b, and 4c) share a common structural motif with C_{2v} symmetry [112]. In these species, both the M atom and the four CO ligands form terminal bonds with the iron atom. These anions exhibit doublet ground states of $^2B_2$ multiplicity.

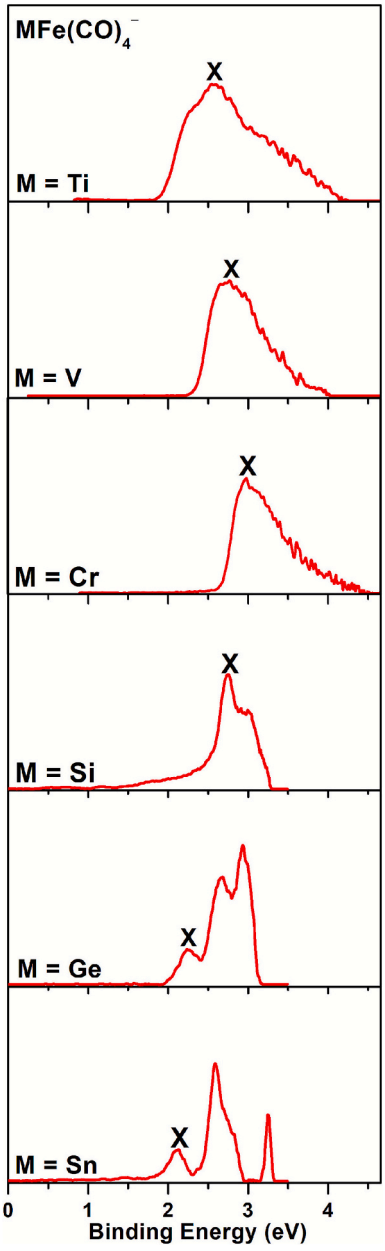

Fig. 5. Photoelectron spectra of $MFe(CO)_4^-$ (M = Ti, V, Cr) recorded at 266 nm (4.661 eV) and $MFe(CO)_4^-$ (M = Si, Ge, Sn) at 355 nm (3.496 eV). Reproduced with permission [111,112].

The calculated *V*DEs and ADEs for these lowest-energy isomers show excellent consistence with the corresponding experimental results. The theoretically determined VDE/ADE values for $MFe(CO)_4^-$ (M = Ti, *V*, Cr, Si, Ge, Sn) anions are as follows: 2.41/2.13, 2.67/2.27, 3.04/2.49, 2.54/1.98, 2.23/1.95, and 2.14/1.95 eV, respectively [111,112]. The close correspondence between the computational and experimental results strongly supports the proposed geometric and electronic structural assignments.

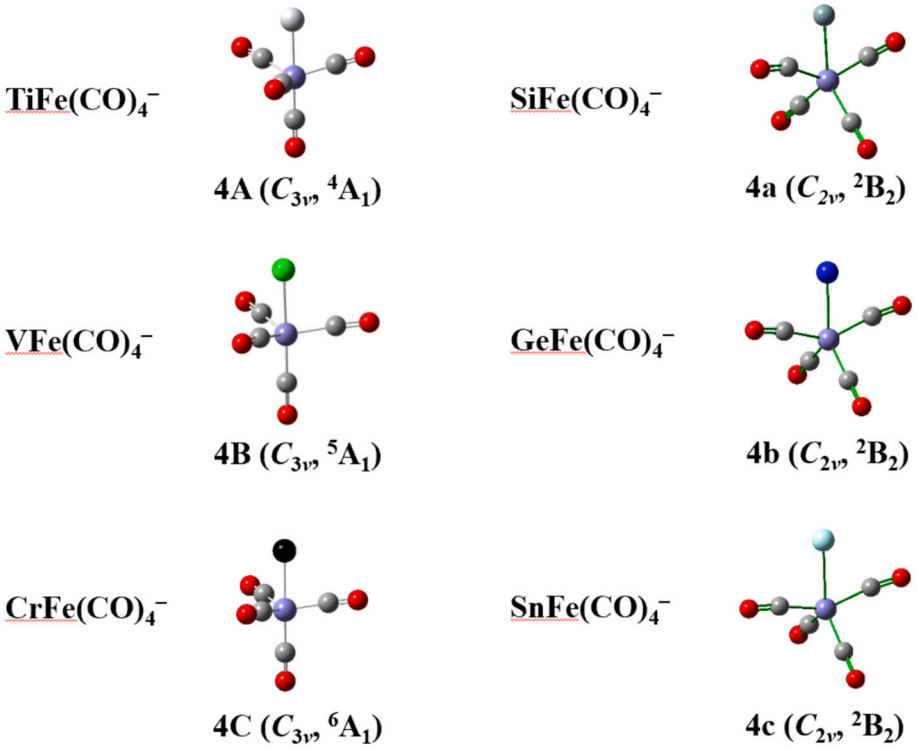

Fig. 6. The most stable structures for $MFe(CO)_4^-$ (M = Ti, V, Cr, Si, Ge, Sn) (Fe, purple). Reproduced with permission [111,112]. (For interpretation of the references to colour in this figure legend, the reader is referred to the web version of this article.)

3.4. $MNi(CO)_n^-$ (*M* = Sc, Y, Ti, Zr, Hf, V; *n* = 3–5)

3.4.1. Photoelectron spectra

The photoelectron results of $MNi(CO)_n^-$ clusters (M = Sc, Y, Ti, Zr, Hf, V; *n* = 3–5) (Figs. 7–9) were recorded using 355 nm (3.496 e*V*). Each spectrum shows a dominant, intense band, labeled as the X band. The VDEs for $MNi(CO)_3^-$ (M = Sc, Y, Ti, Zr, Hf, *V*) were determined from the maxima of these bands and were measured to be 1.83 ± 0.08, 1.89 ± 0.08, 1.93 ± 0.08, 2.04 ± 0.07, 2.09 ± 0.07, and 1.95 ± 0.08 e*V*, respectively [113–115]. Because the spectral bands lack vibrationally resolved fine structure, the ADEs could not be directly measured. Therefore, the ADEs were estimated by extrapolating the leading edge of the dominant photoelectron band to the baseline along the eBE axis. The resulting ADE values for $MNi(CO)_3^-$ (M = Sc, Y, Ti, Zr, Hf, *V*) are 1.68 ± 0.09, 1.69 ± 0.09, 1.83 ± 0.09, 1.86 ± 0.08, 1.91 ± 0.08, and 1.66 ± 0.09 eV, respectively [113–115].

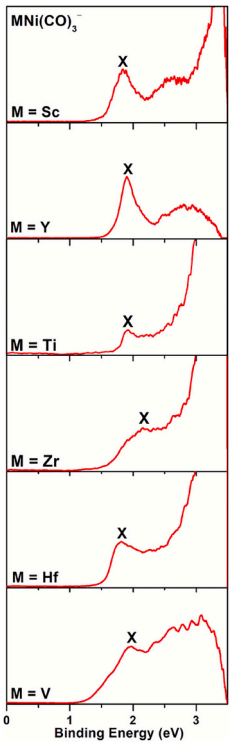

Fig. 7. Photoelectron spectra of $MNi(CO)_3^-$ (M = Sc, Y, Ti, Zr, Hf, V) recorded at 355 nm (3.496 eV) [113–115].

The experimental photoelectron spectra of $MNi(CO)_4^-$ and $MNi(CO)_5^-$ (M = Sc, Y, Ti, Zr, Hf, V) display spectral characteristics similar to those of their tricarbonyl counterparts (Figs. 8–9). The VDE and ADE results for $MNi(CO)_4^-$ (M = Sc, Y, Ti, Zr, Hf, V) were determined to be 1.86 ± 0.08/1.70 ± 0.09, 1.96 ± 0.08/1.72 ± 0.09, 2.56 ± 0.05/2.26 ± 0.06, 2.62 ± 0.04/2.31 ± 0.06, 2.68 ± 0.04/2.40 ± 0.05, and 2.48 ± 0.05/2.22 ± 0.06 eV, respectively [113–115]. Similarly, for $MNi(CO)_5^-$ (M = Sc, Y, Ti, Zr, Hf, V), the measured VDE/ADE values are 1.94 ± 0.08/1.73 ± 0.09, 2.12 ± 0.07/1.73 ± 0.09, 2.98 ± 0.03/2.61 ± 0.04, 3.01 ± 0.02/2.62 ± 0.04, 3.11 ± 0.02/2.67 ± 0.04, and 2.89 ± 0.03/2.70 ± 0.04 e*V*, respectively [113–115]. A consistent trend is observed for all the studied $MNi(CO)_n^-$ anions, and the VDE increases systematically as the cluster size (*n*) grows. This behavior indicates enhanced electronic stabilization with each additional CO ligand, which can be attributed to greater delocalization of the negative charge and stronger metal–ligand interactions in the larger carbonyl complexes.

3.4.2. Comparison between experimental and theoretical results

For density functional theory calculations, the $MNi(CO)_n^-$ (M = Sc, Y) systems have been optimized by B3LYP hybrid functional, whereas the BP86 generalized gradient approximation (GGA) functional was employed for $MNi(CO)_n^-$ (M = Ti, Zr, Hf, *V*) systems. The C and O atoms were described with aug-cc-pVTZ basis set [155], while all metal atoms

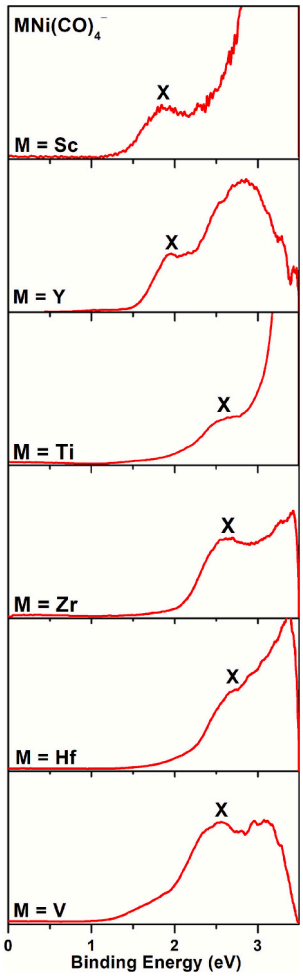

Fig. 8. Photoelectron spectra of $MNi(CO)_4^-$ (M = Sc, Y, Ti, Zr, Hf, V) recorded at 355 nm (3.496 eV) [113–115].

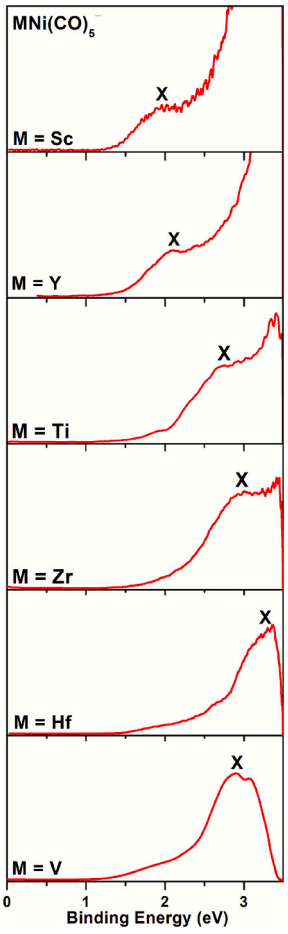

Fig. 9. Photoelectron spectra of $MNi(CO)_5^-$ (M = Sc, Y, Ti, Zr, Hf, V) recorded at 355 nm (3.496 eV) [113–115].

(Sc, Y, Ti, Zr, Hf, V, Ni) were treated with the Stuttgart–Dresden effective core potential (SDD ECP) and its corresponding basis set. The optimized ground-state geometry of $MNi(CO)_n^-$ (M = Sc, Y, Ti, Zr, Hf, V; n = 3–5) are displayed in Fig. 10 [113–115].

For $MNi(CO)_3^-$ (M = Sc, Y, Ti, Zr, Hf), the coordination motifs in the lowest-energy structures include side-on bonding, bridging, and terminal, with terminal CO ligands located exclusively at the Ni center. Their computational VDEs/ADEs for these species are 1.65/1.55, 1.62/1.50, 2.18/2.13, 2.32/2.11, and 2.24/2.02 e*V*, respectively, consistent with their experiments. Distinctively, the global minimum of $VNi(CO)_3^-$ exhibits a structure with three bridging carbonyl ligands. These theoretical VDE and ADE for this anion are 1.80 and 1.59 eV, respectively, which closely match the corresponding experimental observations [113–115].

For the tetra-carbonyl complexes (n = 4), the most stable isomers of $MNi(CO)_4^-$ (M = Sc, Y) have structures featuring two terminal carbonyl ligands, one bridging carbonyl, and one side-on-bonded CO. In these configurations, the terminal CO ligands are coordinated to the Sc and Y centers, respectively. These anions can be considered as derivatives of the corresponding $MNi(CO)_3^-$ species, formed by the terminal addition of a fourth CO connected to the Sc or Y atom. The calculated *V*DEs/ADEs of $MNi(CO)_4^-$ (M = Sc, Y) are 1.76/1.60 and 1.72/1.57 eV, respectively, confirming the experimental data. For the metals Ti, Zr, Hf, and V, the predominant $MNi(CO)_4^-$ isomer features a single terminal carbonyl bound to Ni alongside three bridging CO ligands. Specifically, the $VNi(CO)_4^-$ cluster is formed by the terminal coordination of an additional CO molecule to the Ni center in $VNi(CO)_3^-$. The theoretical VDE/ADE values for $MNi(CO)_4^-$ (M = Ti, Zr, Hf, V) are 2.58/2.23, 2.51/2.15, 2.69/2.44, and 2.59/2.37 e*V*, respectively, all of which closely match the corresponding experimental results [113–115].

For the penta-carbonyl complexes $MNi(CO)_5^-$ (M = Sc, Y, Ti, Zr, Hf), their most stable isomers feature a coordination pattern consisting of one side-on-bonded carbonyl, one bridging carbonyl, and three terminal carbonyl ligands. Among the terminal ligands, one CO is attached to the Ni atom, and the additional two COs are bound to the respective M centers (Sc, Y, Ti, Zr, Hf). The complexes with M = Sc and Y are structurally derived from their $MNi(CO)_4^-$ analogues through the terminal coordination of an additional CO molecule to the Sc or Y atom. The computed *V*DE/ADE values for these systems are 2.06/1.87, 2.00/1.79, 3.10/2.84, 3.21/2.67, and 3.37/2.69 eV, each in well consistent with experiment. The global minimum of $VNi(CO)_5^-$ contains two terminal carbonyl ligands and three bridging carbonyls, with one terminal CO bound to Ni and the other to V. This structure is derived from $VNi(CO)_4^-$ by the terminal attachment of a CO ligand to the V metal atom, and the theoretical VDE (3.13 eV) and ADE (2.89 eV) of $VNi(CO)_5^-$ closely match the experimental values [113–115].

4. Discussion

4.1. $M(CO)_n$ (M = Sc, Y, La)

4.1.1. Geometric and electronic structures

To interpret the experimental IR spectra and elucidate the geometric, electronic, and bonding characteristics of these three neutral complexes, we performed high-level quantum chemical calculations [109]. All computations were conducted within the DFT method, employing the

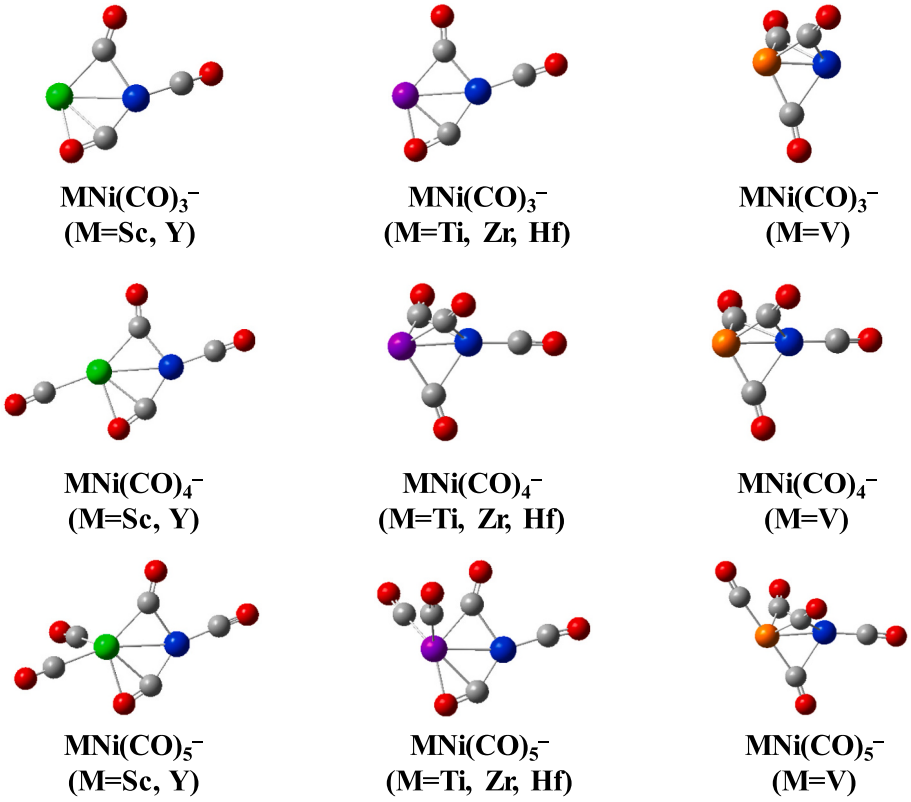

Fig. 10. The most stable structures for $MNi(CO)_n^-$ (M = Sc, Y, Ti, Zr, Hf, V; n = 3–5) (Ni, blue) [113–115]. (For interpretation of the references to colour in this figure legend, the reader is referred to the web version of this article.)

PBE GGA functional and TZ2P basis set. For the lowest-energy isomers for each complex (Fig. 1), the ground-state of $Sc(CO)_7$ is a doublet ($^2B_2$) with C_{2v} symmetry, and the structure features seven terminal CO ligands coordinated around the central scandium atom in a geometry that maximizes metal–ligand interactions while minimizing steric repulsion. The optimized geometry exhibits distinct Sc—C bond lengths and C–Sc–C bond angles, reflecting an asymmetric distribution of carbonyl ligands around the metal center. This asymmetry accounts for the experimentally observed multiplicity of IR bands. In contrast, the neutral $Y(CO)_8$ and $La(CO)_8$ complexes exhibit eightfold coordination. Initial optimizations suggested structures with ideal O_h symmetry; however, the open-shell doublet electronic configuration, featuring a SOMO, introduces electronic instability and triggers the Jahn–Teller effect [156]. This effect causes a dynamic distortion from the ideal octahedral geometry, leading to energetically stabilized structures of lower symmetry. In consequence, the refined ground-state configurations of both $Y(CO)_8$ and $La(CO)_8$ exhibit D_{4h} symmetry, in which such distortion eliminates the degeneracy of the frontier orbitals and imparts energetic stabilization to the complexes.

Calculated vibrational frequencies of the optimized geometries closely match the experimental IR spectra, verifying that the identified isomers represent their potential energy surfaces of the global minima. Natural bond and molecular orbital analyses reveal significant π back-donation of occupied metal d orbitals to the π* orbitals, thus accounting for the observed red shifts. Furthermore, the calculated M–C bond lengths and stretching force constants show systematic trends across the three neutral species, mirroring the evolving equilibrium between π-back-donation and σ-donation. This modulation results from the increasing radial extent and decreasing energy of the metal valence orbitals, and key factors that dictate the efficiency metal–ligand bonding interactions [157].

4.1.2. Orbital and bonding analysis

The metal–CO bonding schemes for the three neutral complexes are shown in Fig. 11 and the corresponding three-dimensional isosurfaces of their molecular orbitals (MOs) in Fig. 12, respectively [109]. For $Sc(CO)_7$ (Fig. 11A), bonding primarily stems from interactions between the scandium atomic orbitals (4 s, 3d, 4p) and the 5σ orbitals of the seven carbonyl ligands. These interactions form the valence molecular orbitals, including nine occupied MOs that mediate bonding between Sc and the CO ligands. Analysis of the frontier MOs, which are key to the bonding and electronic structure of the complex, unveils that the LUMO ($11b_1$), SOMO ($8b_2$), and HOMO ($13a_1$) are all of predominant π-bonding character. These orbitals arise from interactions between the Sc 3d orbitals (approximately 33%) and the 2π* orbitals of the CO ligands. This π-bonding nature underscores that metal–ligand bonding in this complex is largely governed by back-donation from the Sc 3d orbitals into the CO 2π* orbitals. The energy separation between the SOMO and LUMO is approximately 1.4 eV, reflecting a relatively stable electronic structure [158]. The magnitude of the SOMO–LUMO gap is a key indicator of the complex's electronic stability: a larger gap typically means higher vertical excitation energy and greater ground state stability. Orbitals labeled HOMO-1 ($10b_1$), HOMO-2 ($6a_2$), HOMO-3 ($12a_1$) possess σ bonding MOs, formed from interactions between Sc 3d orbitals (10–14% contribution) and the ligand 5σ orbitals, providing supplementary stabilization. The remaining MOs (9_{b1}, 11_{a1}, 7_{b2}, and 8_{a1}) are localized on the ligand framework (>92% CO contribution) and show weak σ-bonding character involving Sc 4 s/4p and ligand 5σ orbitals. Overall, the bonding analysis indicates that the primary stabilization of the $Sc(CO)_7$ complex arises from interactions involving the Sc 3d orbitals and the ligand MOs, with π back-donation from Sc to CO playing a particularly important role.

The neutral $Y(CO)_8$ has a higher coordination number [109], resulting in a more complex electronic structure with ten occupied MOs (Fig. 11B). The bonding between metal and ligands can be thoroughly

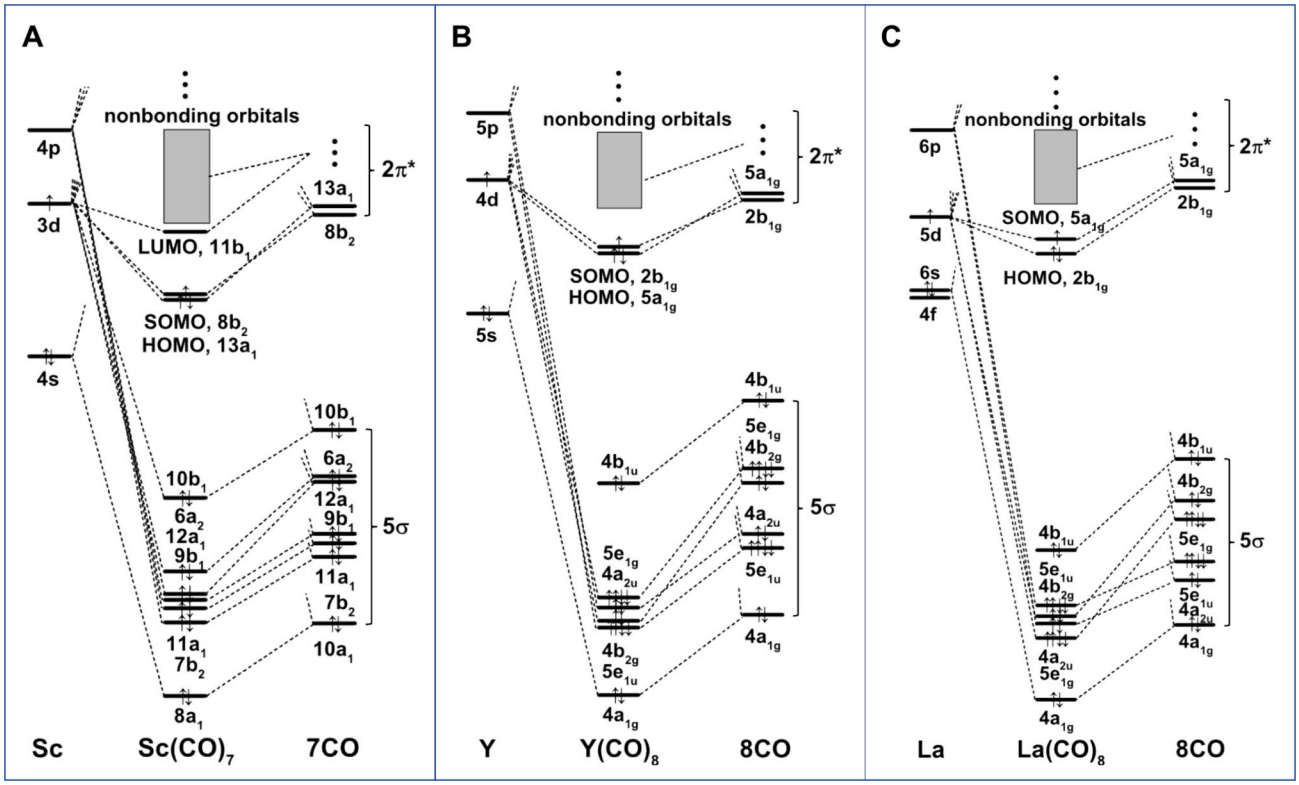

Fig. 11. The bonding schemes of (A) $Sc(CO)_7$, (B) $Y(CO)_8$, and (C) $La(CO)_8$. Reproduced with permission [109].

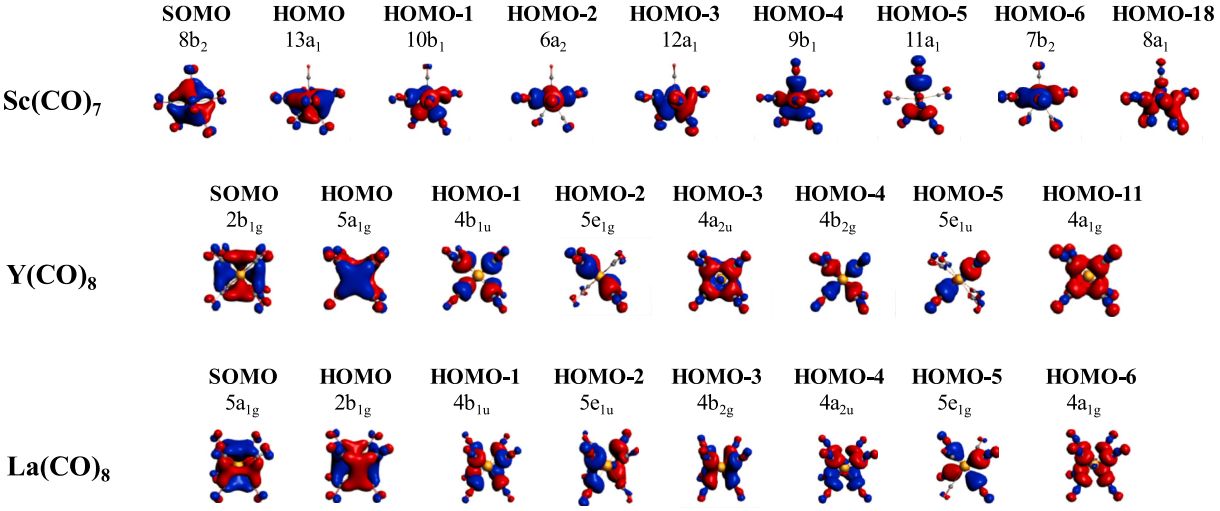

Fig. 12. The 3D isosurfaces (isovalue = 0.03) of the occupied orbitals related to metal-CO bonding of $Sc(CO)_7$, $Y(CO)_8$, and $La(CO)_8$ [109].

examined through orbital interactions. Arising from 2π* orbitals of the ligand $(CO)_8$, the frontier empty MOs are largely nonbonding in character. Additionally, the SOMO and HOMO ($2b_{1g}$, $5a_{1g}$) exhibit substantial contributions from both the 4d atomic orbitals (AOs) of Y, and the 2π* MOs of the $(CO)_8$ ligands. HOMO-1 ($4b_{1u}$) is a purely ligand-based orbital, highlighting its strong ligand-only nature. The HOMO-2 and HOMO-4 ($5e_{1g}$, $4b_{2g}$) orbitals are σ-bonding MOs formed by effective overlap between Y 4d and ligand 5σ orbitals. These σ-type interactions contribute substantially to overall stability. The Y 5p AOs participate only minimally (~3%) in the formation of HOMO-3 and HOMO-5 ($4a_{2u}$, $5e_{1u}$), owing to their relatively high energy and poor overlap with ligand orbitals. In contrast, the Y 5 s atomic orbital plays a more considerable role in bonding, contributing approximately 14% to HOMO-11 ($4a_{1g}$) orbital composition. This increased involvement arises from more effective spatial overlap and better energy alignment in the D_{4h} point group symmetry adopted by the $(CO)_8$ ligand field. This detailed orbital analysis not only clarifies the bonding characteristics of $Y(CO)_8$ but also emphasizes how the central metal's identity and coordination geometry collectively shape their electronic structures of these complexes.

The bonding configuration in $La(CO)_8$ (Fig. 11C) closely resembles that of $Y(CO)_8$, mainly owing to their identical coordination numbers [109]. However, subtle differences appear in the MO energy ordering. In $La(CO)_8$, the HOMO-7 ($4a_{1g}$) orbital lies below the $5e_{1g}$ orbital, a slight inversion compared to $Y(CO)_8$. This shift results from the distinct electronic properties of La versus Y. Additionally, the gap of SOMO–LUMO

in $La(CO)_8$ is approximately 1.0 eV, slightly smaller than the 1.4 eV gap in $Y(CO)_8$. This reduced gap reflects a more complex MO manifold in $La(CO)_8$, indicating increased complexity in metal–ligand interactions. Notably, the relative energetic ordering of the HOMO and SOMO is inverted between Y and La complexes, and a feature explainable by variations in the metal d-orbital contributions to these frontier MOs.

4.1.3. Energy and stability analysis

The metal–carbonyl bonding interactions in these three neutral species were probed via EDA-NOCV method [109]. This sophisticated technique allows for a detailed quantitative breakdown of how fragment molecular orbitals to the overall bond. Specifically, the total interaction energy (ΔE_{int}) separating metal fragment and $(CO)_n$ ligands set is partitioned into three principal terms: Pauli repulsion (ΔE_{Pauli}), electrostatic attraction (ΔE_{elstat}), and orbital interaction ($\Delta E_{orbital}$).

EDA-NOCV analysis indicates that the bonding in these group 3 carbonyls is primarily covalent in character. Specifically, the orbital interaction term $\Delta E_{orbital}$ contributes approximately 62% of these total attractive interactions, while the electrostatic component ΔE_{elstat} accounts for the remaining 38%. This highlights the importance of covalent bonding, driven by synergistic π-back-donation and σ-donation, in stabilizing these complexes. A distinct trend is evident in the $\Delta E_{orbital}$ values, decreasing in the order Sc > Y > La, indicating that covalent bonding is strongest in the scandium complex. This trend stems from the relative energies of the d orbitals, and the Sc 3d orbitals lie lower than Y 4d and La 5d orbitals, allowing better energetic alignment with the CO frontier molecular orbitals, which enhances orbital overlap and strengthens the covalent interactions.

Complementary Mayer bond order calculations for the metal–carbonyl bonds support the EDA-NOCV analysis [109]. The bond orders follow a consistent trend: Sc–C > Y–C > La–C, which directly correlates with the observed decrease in $\Delta E_{orbital}$. This gradual decline in bond order down the group reflects a weakening of the crucial back-donation (M → CO), an essential aspect of metal–CO bonding. Together, these electronic structure insights provide a unified mechanistic explanation for the spectroscopic trends: the reduction in covalent bond strength, especially in π-back-donation yields a less pronounced red shift relative to free CO across the series Sc > Y > La compared to free CO. This clear correlation firmly establishes that the electronic structure dictates the vibrational properties of metal–carbonyl complexes.

Theoretical thermodynamic calculations for the dissociation reactions $M(CO)_8 \rightarrow M(CO)_7 + CO$ (M = Sc-La) support the electronic structure analyses (Table 1) [109]. Both ΔH and ΔG show a clear monotonic increase along the series Sc → Y → La, indicating a gradual thermodynamic destabilization of the carbonyl complexes as the metal atomic number increases. Importantly, ΔG for $Sc(CO)_8$ dissociation becomes negative near 200 K, revealing spontaneous decomposition to $Sc(CO)_7$ and CO at cryogenic temperatures. This suggests that under higher temperatures, the formation of $Sc(CO)_8$ from $Sc(CO)_7$ and CO is not spontaneous. Conversely, the ΔG values for the corresponding dissociation reactions of $Y(CO)_8$ and $La(CO)_8$ remain positive across the relevant temperature range, confirming that these octacarbonyl complexes are thermodynamically more stable than the Sc analogue. Notably, the low temperatures (~200 K) are sufficient for the potential formation of $Sc(CO)_7$. Furthermore, the thermodynamic instability of $Sc(CO)_8$ under the experimental conditions offers a plausible reason for its absence in the spectra. In contrast, the detected spectral signals of $Y(CO)_8$ and $La(CO)_8$ reflect their excellent thermodynamic stability. These findings highlight the importance of simultaneously considering electronic structure and thermodynamic stability when predicting the viability and experimental detectability of metal carbonyl species.

Table 1
The changes of enthalpy (ΔH, kcal/mol) and Gibbs free energy (ΔG, kcal/mol) of the $M(CO)_8 \rightarrow M(CO)_7 + CO$ (M = Sc, Y, La) reactions calculated at the PBE/TZ2P level of theory. Reproduced with permission [109].

T (K)	$Sc(CO)_8 \rightarrow Sc(CO)_7 + CO$		$Y(CO)_8 \rightarrow Y(CO)_7 + CO$		$La(CO)_8 \rightarrow La(CO)_7 + CO$	
	ΔH	ΔG	ΔH	ΔG	ΔH	ΔG
0	5.15	5.15	12.57	12.57	13.43	13.43
100	5.72	1.75	13.04	8.94	13.51	10.53
200	5.87	−2.28	13.05	4.8	13.16	7.68
298.15	5.88	-6.31	12.9	0.79	12.71	5.1

4.2. $OTiCC(CO)_n$

4.2.1. Geometric and electronic structures

For these different isomers (Fig. 4), the Ti coordination shell is effectively saturated at $n = 4$, whereas in the $n = 5$ complex, the additional CO is physiosorbed at a secondary coordination site [110]. This behavior suggests that the $OTiCCO(CO)_n$ motif imposes both steric and electronic constraints that limit the primary coordination number to six. The second structural type consists of conventional homoleptic complexes, $Ti(CO)_{n+2}$, in which the titanium atom is coordinated exclusively by terminal CO ligands.

Analysis of the relative energies shows that for smaller complexes ($n = 2$ and 3), greater stability is found for the $OTiCCO(CO)_n$ isomers as compared to the homoleptic $Ti(CO)_{n+2}$ structures [110]. In contrast, for larger complexes ($n = 4$ and 5), the homoleptic isomers become energetically favored. This shift in stability with increasing ligand number highlights the delicate balance between steric effects, electronic stabilization, and the degree of metal-to-ligand back-donation in determining the preferred bonding configuration. To further validate the structural assignments, the infrared spectra of both isomeric forms of the $n = 5$ complex were simulated and rigorously compared with the experimentally measured IR spectrum. The results show an excellent match between the predicted and experimental spectrum of $OTiCCO(CO)_5$, both in band positions and relative intensities, unambiguously confirming it as the predominant species under the experimental conditions.

4.2.2. Orbital and bonding analysis

The OTiCCO geometry is computed to possess its ground state with a closed-shell singlet ($^1A'$) [110]. Structurally, it adopts a planar but bent geometry, featuring an acute O–Ti–C bond angle of 111.8°. The theoretical Ti—C bond distance of 1.889 Å closely corresponds to the expected value for a formal Ti═C double bond based on covalent radii, indicating substantial multiple-bond character [159]. Further insights into the electronic structure were obtained through analysis of the valence MOs. The HOMO can be described as a π orbital that is localized on the CCO unit and possesses in-plane symmetry, analogous to the SOMO of the triplet ground state ($^3\Pi$) of the free CCO radical. These orbital exhibits bonding character between the C—C atoms and antibonding character between the C—O atoms.

The HOMO-1 possesses an out-of-plane π orbital formed by d_δ/CCO-π hybridization (denoted as SOMO') [110]. This orbital displays considerable Ti—C bonding character and serves as the primary electronic factor responsible for the bent molecular geometry (O–Ti–C angle 111.8°). The HOMO-2 and HOMO-3 are assigned as π-bonding orbitals between Ti and O in and vertical to molecular plane, respectively, while the HOMO-4 corresponds to σ-bonding orbital of Ti—O. while HOMO-5 is essentially a σ-type lone pair orbital localized on the CCO fragment, which participates in weak donor–acceptor interactions with the TiO unit. Based on these bonding features, the ground state of OTiCCO has been described as a bonding interaction between doublet TiO^+ ($^2\Delta$) and doublet CCO^- ($^2\Pi$). This interaction generates a delocalized electron-sharing π bond, providing a consistent explanation for both the bent geometry and the stabilization of the closed-shell singlet ground state.

4.2.3. Reaction process and stability analysis

The reaction energetics for Ti + CO association and subsequent

complex growth were evaluated at the B2PLYP-D3/def2-TZVPP level of theory [110]. The initial step, The ΔH of Ti + CO → TiCO is predicted to be +2.6 kcal·mol^{-1}, which indicates slightly endothermic. The ΔH of TiCO + CO → Ti(CO)$_2$ is −39.2 kcal·mol^{-1}, which is strongly exothermic. Analysis of the potential energy surface for Ti + 2CO → OTiCCO (Fig. 13) reveals a highly exothermic overall process with only a small kinetic barrier of approximately 1.0 kcal·mol^{-1} above the reactants. The triplet-state of Ti(CO)$_2$ isomer is less stable by 37.0 kcal·mol^{-1} relative to the OTiCCO isomer, clearly confirming the thermodynamic preference for OTiCCO formation. These results demonstrate that the pathway Ti + 2CO → OTiCCO is shown to be both thermodynamically favored and kinetically accessible in the gas phase.

Importantly, collisional cooling in the molecular beam fails to stabilize the TiCO/Ti(CO)$_2$ intermediates, thus allowing Ti(CO)$_2$ to readily isomerize to OTiCCO under the current experimental conditions. Larger complexes, OTiCCO(CO)$_n$, form via sequential exothermic CO additions to smaller precursors, with reaction enthalpies of −21.4, −18.8, −14.8, −3.6, and − 1.5 kcal·mol^{-1} for n = 1–5. Experimentally, the bare Ti(CO)$_{n+2}^{+}$ ions (n = 4, 5) are absent despite their predicted thermodynamic stability over OTiCCO(CO)$_n$ isomers, which is due to the unavailability of gas-phase Ti(CO)$_{n+2}$ precursors with adequate stability. Overall, the computational results strongly support OTiCCO formation as the dominant pathway in Ti + CO reactivity.

4.3. $MFe(CO)_4^-$ (M = Ti, V, Cr, Si, Ge, Sn)

4.3.1. Geometric and electronic structures

The structures of the MFe(CO)$_4^-$ complexes (M = Ti, *V*, Cr, Si, Ge, Sn) have been clearly determined, showing excellent agreement between experimental and theoretical spectra [111,112]. These anions adopt a geometry with all four CO bound terminally to iron, and the metal atom directly coordinated with the iron center. A clear structural dichotomy emerges: group 14 elements (M = Si, Ge, Sn) preferentially adopt C_{2v} symmetric structures, whereas early transition metals (M = Ti, *V*, Cr) favor C_{3v} symmetry. This difference reflects fundamental variations in the electronic properties and bonding characteristics of the M atoms.

Previous studies on related systems, including ZnFe(CO)$_4^-$, PbFe(CO)$_4^-$, CdFe(CO)$_4^-$, and HgFe(CO)$_4^-$, have consistently shown that these complexes maintain a structural framework based on the iron tetracarbonyl unit [126–128]. This indicates that the MFe(CO)$_4^-$ configuration, with an intact Fe(CO)$_4$ unit, represents a particularly stable structural motif. As summarized in Table 2 [111,112], the natural charge reveals that M atom is the primary locus for both positive charge and unpaired electron density. For these metals Ti, *V*, Cr, the spin

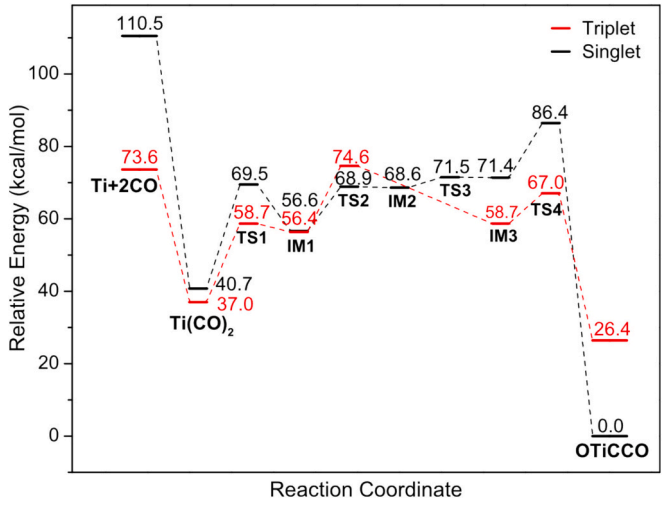

Fig. 13. Potential energy profiles of the Ti + 2CO → OTiCCO reaction calculated at the B2PLYP-D3/def2-TZVPP level of theory [110].

Table 2
M − Fe bond lengths, Wiberg bond orders and natural charges of MFe(CO)$_4^-$ (M = Ti, V, Cr, Si, Ge, Sn) species. Reproduced with permission [111,112].

Species	M − Fe bond length	M − Fe Wiberg bond order	Natural charge	
			M	Fe
TiFe(CO)$_4^-$	2.42	0.67	0.42	−2.05
VFe(CO)$_4^-$	2.39	0.64	0.37	−2.05
CrFe(CO)$_4^-$	2.44	0.52	0.38	−2.08
SiFe(CO)$_4^-$	2.26	0.91	0.43	−2.29
GeFe(CO)$_4^-$	2.37	0.89	0.34	−2.34
SnFe(CO)$_4^-$	2.58	0.83	0.31	−2.35

density is almost exclusively localized on M, while the Fe(CO)$_4$ fragment carries a natural charge of approximately −2e. This is further supported by Mulliken spin density calculations (Table 3), which give values of 3.11, 4.23, and 5.33 for Ti, V, and Cr, respectively, highlighting the considerable radical character of the M atom. These electronic structure characteristics implies substantial M → Fe(CO)$_4$ electron transfer, giving a formal oxidation state of M(I) and Fe(−II). The MFe(CO)$_4^-$ complexes (M = Ti, V, Cr) have been described as M^+ interacting with $[Fe(CO)_4]^{2-}$. In contrast, the natural charges on the Fe(CO)$_4$ fragment of the group 14 elements (M = Si, Ge, Sn) are calculated as −1.43, −1.34, and − 1.31, respectively, while the iron atom maintains a charge near −2.30 across the series. This distribution supports an alternative description in which these complexes are best represented as containing a $[M]^0[Fe(CO)_4]^-$ ion core. In this configuration, the iron atom achieves a stable 18-electron configuration, which greatly enhances the thermodynamic stability of these complexes [160].

4.3.2. Orbital analysis

Fig. 14 presents the frontier molecular orbital profiles for the most stable isomers of the anionic heterobimetallic carbonyl complexes MFe(CO)$_4^-$ (M = Ti, *V*, Cr, Si, Ge, Sn) [111,112]. Specifically for the TiFe(CO)$_4^-$ complex, analysis shows that both the HOMO and HOMO-1 possess singly occupied orbitals with predominant localization on the titanium center. These orbitals are essentially nonbonding, with approximately 90% contribution from Ti 3d AOs. The HOMO-2 is also a singly occupied orbital, consisting of a hybrid nonbonding orbital with contributions from Ti 3d (35%), 4 s (47%), and 4p (12%) orbitals. Nearly degenerate and doubly occupied orbitals have been found in HOMO-3 and HOMO-4. These orbitals are primarily derived from Fe 3d orbitals and exhibit considerable back-donation interactions with CO ligands. The HOMO-5 is a doubly occupied Ti—Fe σ-bonding orbital, arising from the overlap of hybrid orbitals on both metals: Fe 3d and 4p (13% and 30%, respectively) and Ti 3d and 4 s (8% and 18%, respectively). In VFe(CO)$_4^-$, the four highest orbitals (HOMO through HOMO-3) are all singly occupied and nonbonding, with primary localization on the vanadium atom, with V 3d contributions of 83%, 72%, 95%, and 65%, respectively. Doubly occupied and nearly degenerate orbitals have been also found in HOMO-4 and HOMO-5. These orbitals are mainly of Fe 3d character and facilitate back-donation to the CO π* system. In CrFe(CO)$_4^-$ anion, five singly occupied orbitals are present from HOMO to HOMO-4, all exhibiting nonbonding character with considerable

Table 3
Contributions of the unpaired spin density distributions in the MFe(CO)$_4^-$ (M = Ti, V, Cr, Si, Ge, Sn) species. Reproduced with permission [111,112].

Species	Spin density of M	*n*s	*n*p	*n*d
TiFe(CO)$_4^-$	3.11	21%	4%	75%
VFe(CO)$_4^-$	4.23	13%	5%	82%
CrFe(CO)$_4^-$	5.33	10%	3%	87%
SiFe(CO)$_4^-$	0.63	2%	98%	0%
GeFe(CO)$_4^-$	0.85	5%	95%	0%
SnFe(CO)$_4^-$	0.97	0%	100%	0%

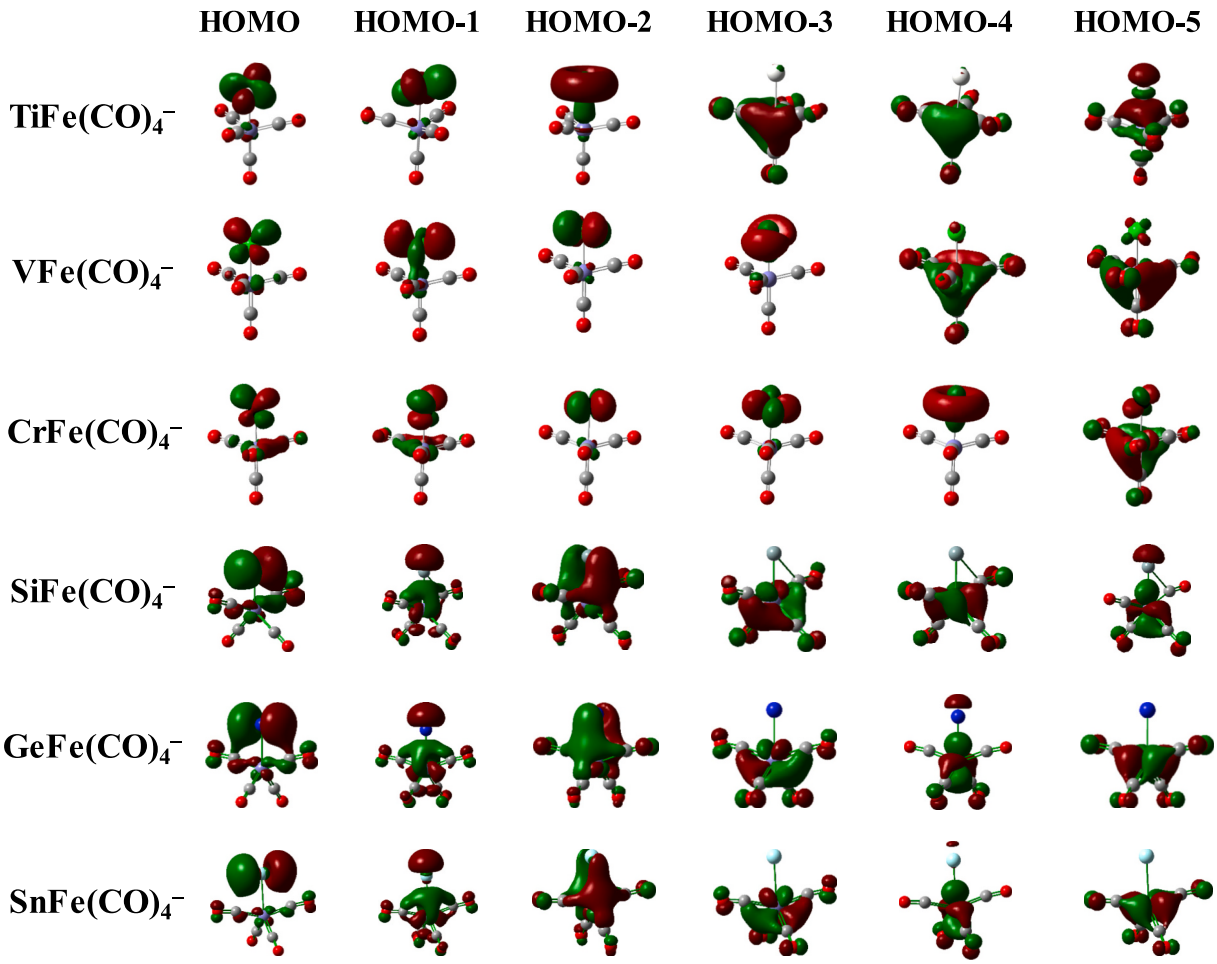

Fig. 14. Molecular orbital pictures of the most stable isomers for $MFe(CO)_4^-$ (M = Ti, V, Cr, Si, Ge, Sn), showing the highest occupied molecular orbitals down to the fifth valence molecular orbital from the HOMO [111,112].

localization on the chromium center. The Cr 3d contributions to these orbitals are 70%, 70%, 96%, 96%, and 65%, respectively, and Fe → CO π-back-donation is revealed in degenerate HOMO-5 and HOMO-6 orbitals.

The HOMO of $MFe(CO)_4^-$ (M = Si, Ge, Sn) is primarily localized on the metal atom, with considerable contributions from the *n*p orbitals, increasing from 50% for Si 3p to 68% for Ge 4p and 81% for Sn 5p, reflecting greater orbital localization down the group. The doubly occupied HOMO-1 exhibits σ-bonding character between the metal centers, resulting from the overlap of hybrid orbitals comprising the *n*s and *n*p orbitals of M and the 3d and 4p orbitals of Fe. Notably, the HOMO-3 orbitals in these complexes represent typical π back-donation motifs, with electrons from the filled 3d and 4p orbitals of Fe donated into the vacant *n*p orbitals of M. This interaction strengthens the metal–metal bond, thereby stabilizing the complex. The remaining MOs (HOMO-4 to HOMO-5) primarily arise from interactions between Fe and the CO ligands. Therefore, the M–Fe bond comprises a σ-bond by electron sharing and a dative π-bond (Fe → M).

4.3.3. *Bonding and charge analysis*

A systematic comparison of M–Fe Wiberg bond indices, bond distances, and natural charges reveals a strong dependence on the nature of the ancillary metal M [111,112]. The calculated M–Fe bond lengths cover a wide range, from 2.26 Å in $SiFe(CO)_4^-$ to 2.58 Å in $SnFe(CO)_4^-$. In the M = Ti, *V*, Cr series, the bond lengths are relatively uniform, varying only between 2.39 and 2.44 Å, with the shortest bond found in $VFe(CO)_4^-$. In contrast, complexes containing group 14 elements display considerably greater variability, with M–Fe bond lengths increasing markedly down the group from Si to Sn. This trend parallels the increase in atomic radii down group 14. Notably, the Si—Fe bond is the shortest among all complexes studied, indicating an especially strong bonding interaction [4,161,162]. The Wiberg bond orders, which quantify bond multiplicity and covalent character, are considerably higher for these complexes, ranging from 0.83 to 0.91, compared with the transition metal (TM) analogues, which lie between 0.52 and 0.67. The maximum value of Wiberg bond order is 0.91 in $SiFe(CO)_4^-$, reflecting by its short bond length and signaling a highly covalent M–Fe interaction [163–165]. Among these TM anions, the bond orders diminish in the sequence Ti > *V* > Cr, indicating a gradual reduction in bond strength. These computational findings unravel a fundamental difference in bonding character between transition metal and group 14-based heterobimetallic carbonyl complexes, stemming from variations in electronic structure, orbital overlap, and charge distribution in the M–Fe bond.

Natural population analysis (NPA) reveals considerable charge separation in these heterobimetallic carbonyl anions [111,112]. The iron center consistently carries a large negative charge, ranging from −2.00 to −2.30, indicating substantial accumulation of electron density. At the same time, the ancillary metal atom M exhibits positive charges, varying from +0.31 (Sn) to +0.43 (Si). Notably, the more electronegative group 14 elements (Si and Ge) possess higher positive charges than their TM counterparts, reflecting differences in electronic structure and charge-transfer behavior. The data reveal two distinct bonding regimes between TM and main-group derivatives. Group 14 elements, particularly silicon, form shorter bonds with higher Wiberg bond orders toward iron, indicative of bonding interactions dominated by covalent character. In contrast, complexes with a TM at the metal site exhibit longer bond

lengths and lower bond orders, indicative of more polarized interactions. The unpaired spin density in $MFe(CO)_4^-$ (M = Ti, *V*, Cr, Si, Ge, Sn) resides primarily on the M atom (Fig. 15). In summary, this work provides fundamental understanding the electronic structure and stability of these anions, thereby establishing the identity of the ancillary metal as a key determinant of bonding and charge distribution in bimetallic carbonyl complexes.

4.3.4. CO activation

The structural parameters of the anionic heterobimetallic carbonyl complexes $MFe(CO)_4^-$ (M = Ti, V, Cr) were derived from calculations performed at the BP86/6–311 + G(d)-SDD level of theory. The computed C—O bond distances average around 1.18 Å, reflecting a considerable elongation relative to free CO (1.13 Å at the same level). Consistent with this structural change, the calculated C—O stretching frequencies (1810–1920 cm^{-1}) show a pronounced red shift in contrast to free CO (2121 cm^{-1}). These results collectively indicate a considerable weak C—O bond upon coordination to the bimetallic core. The Group 14 analogues $MFe(CO)_4^-$ (M = Si, Ge, Sn) exhibit similar behavior. As the central atom M descends from Si to Sn, the ∠C1–Fe–C2 bond angle increases from 139° to 150°, while the opposite ∠C3–Fe–C4 angle shows a smaller increase from 101° to 105°. At the same time, the C1—O bond length decreases from 1.181 to 1.163 Å, although it remains considerably longer than in free CO. This structural evolution indicates a gradual loosening of the complex geometry as the atomic radius of M increases, accompanied by weaker M–Fe interactions. The degree of CO activation is reflected by C—O bond elongation and vibrational red shifts. The systematic elongation of C—O bonds and the corresponding decrease in stretching frequencies across both TM and main-group $MFe(CO)_4^-$ complexes highlight a general weakening of the CO bond upon coordination. This behavior parallels CO chemisorption on TM surfaces [27], where comparable red shifts (ca. 1100–2000 cm^{-1}) arise from the same physical origin: significant π-back-donation to the CO ligand. These findings deepen the molecular-level understanding of CO activation in heterometallic carbonyl systems. These insights are relevant to catalytic processes involving CO, such as Fischer–Tropsch synthesis and CO_2 reduction, and underscore the value of integrating theoretical and experimental approaches to elucidate metal–ligand interactions and their catalytic implications.

4.4. $MNi(CO)_n^-$ (M = Sc, Y, Ti, Zr, Hf, V; n = 3–5)

4.4.1. Geometric and electronic structures

The congruence between experimental data and computational predictions affords a reliable physical property of the $MNi(CO)_n^-$ clusters (M = Sc, Y, Ti, Zr, Hf, V; *n* = 3–5). In each element group, the bonding of carbonyl ligands to the Ni atom is remarkably consistent. Comparisons across different transition metal–nickel (M–Ni) carbonyl complexes reveal both similarities and differences in their bonding behavior and growth patterns. Structurally, the group 3 and 4 M–Ni tricarbonyl anions feature three distinct types of carbonyl coordination: side-on-bonded, bridging, and terminal ligands [113,114]. These systems represent the smallest metal carbonyl clusters known to incorporate all major modes of metal–carbonyl coordination. Notably, the $VNi(CO)_3^-$ cluster shows a strong tendency to form three bridging carbonyl ligands [115].

For Group 3 M–Ni carbonyls (M = Sc, Y), the governing structural evolution involves the stepwise addition of terminal CO ligands to the ancillary metal (M) of the key $MNi(CO)_3^-$ motif. This reflects the pronounced stability of the $MNi(CO)_3^-$ structure, with subsequent CO binding preferentially taking place at the Sc/Y sites [113]. In contrast, group 4 M–Ni systems (M = Ti, Zr, Hf) follow a different growth pattern. While the $MNi(CO)_3^-$ and $MNi(CO)_5^-$ anions are similar to their group 3 counterparts, the tetra-carbonyl species $MNi(CO)_4^-$ shows a distinct structural preference, featuring μ-CO ligands and one terminal carbonyl coordinated to the Ni atom [114]. Similarly, the structural evolution of $VNi(CO)_n^-$ (*n* = 3–5) begins with the $VNi(CO)_3^-$ core, which contains only bridging carbonyls. Because the Ni atom initially lacks a terminal carbonyl ligand, subsequent CO adsorption first occurs at the Ni site to form a terminal carbonyl, followed by adsorption at the *V* atom [115]. These mechanistic insights into structural diversification guide our understanding of CO chemisorption on bimetallic surfaces and enable the rational design of catalysts via targeted transition metal selection for CO activation.

4.4.2. Orbital analysis

The frontier molecular orbitals were systematically characterized for the anionic $MNi(CO)_5^-$ complexes with M = Sc, Y, Ti, Zr, Hf, *V* (Fig. 16) [113–115]. For the Sc and Y systems in their global minimum structures, the HOMO, HOMO-1, and HOMO-2 are π-symmetry orbitals delocalized across the metal–carbon framework and thus exhibit bonding interactions between the CO and M atoms. In contrast, the HOMO-3 and

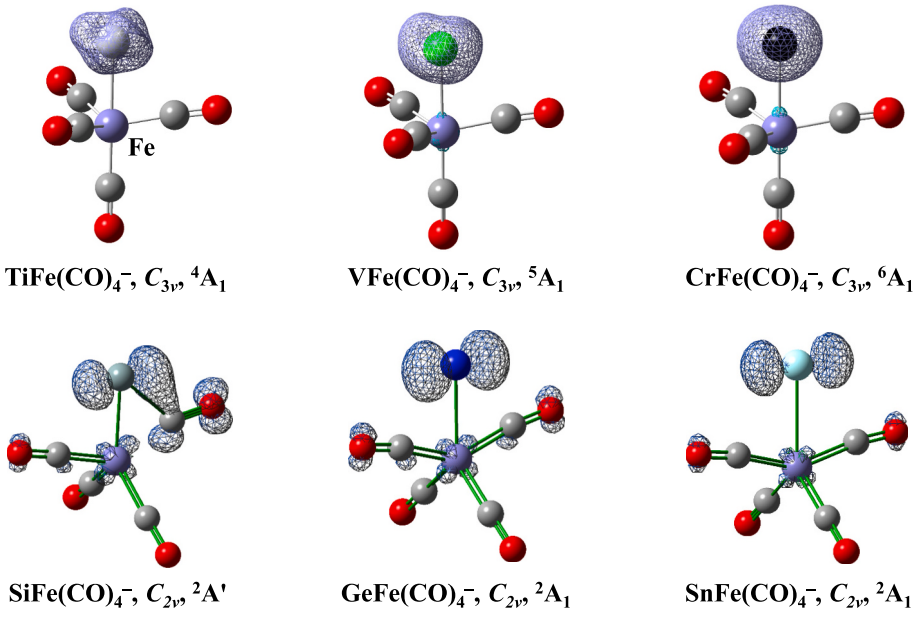

Fig. 15. Isosurface map of unpaired spin density distributions for the most stable isomers of $MFe(CO)_4^-$ (M = Ti, V, Cr, Si, Ge, Sn) [111,112].

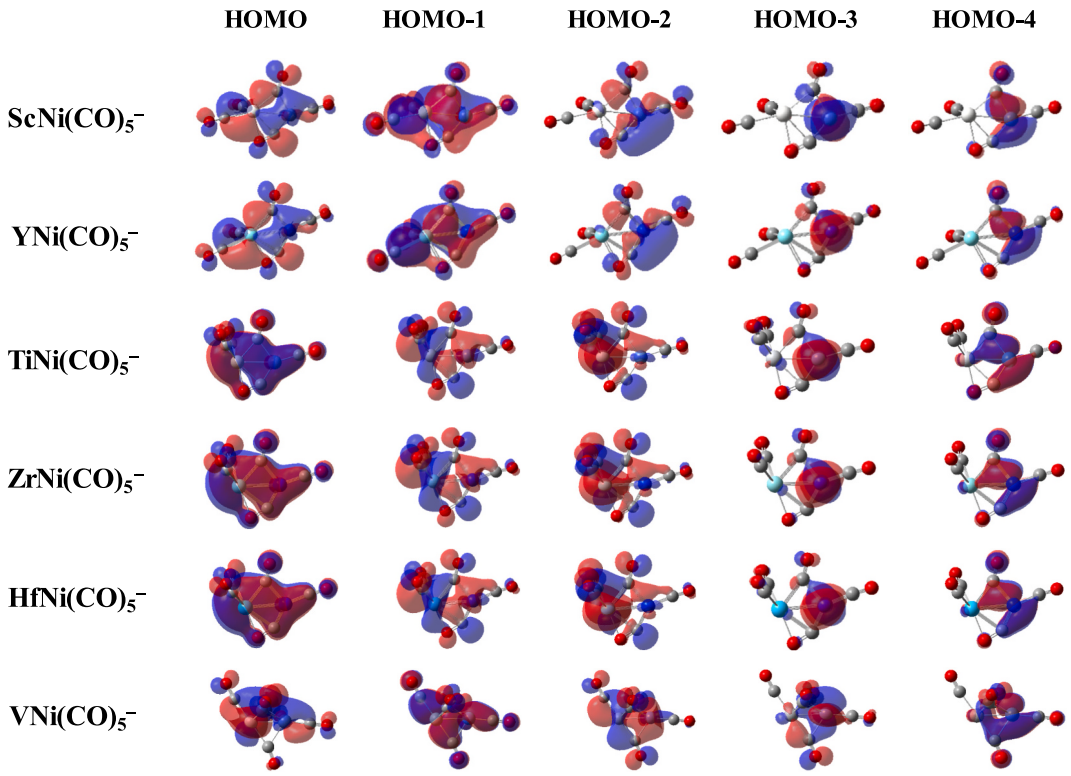

Fig. 16. Molecular orbital pictures of the most stable isomers for $MNi(CO)_5^-$ (M = Sc, Y, Ti, Zr, Hf, V), showing the highest occupied molecular orbitals down to the fourth valence molecular orbital from the HOMO [113–115].

HOMO-4 are primarily derived from the Ni 3d AOs. A similar orbital pattern is observed in the Ti, Zr, and Hf analogues. Specifically, their HOMO orbitals feature significant π-donation of the metal (Ti, Zr, Hf) to the carbonyl ligands. The HOMO-1 and HOMO-2 are π orbitals delocalized across the bimetallic core, while the HOMO-3 and HOMO-4 remain largely confined on the Ni 3d orbitals. However, for the *V*Ni $(CO)_5^-$ cluster, the electronic structure is different. The HOMO and HOMO-2 are primarily localized between the V and Ni atoms, indicating substantial overlap of V and Ni d orbitals, consistent with direct metal–metal bonding. The HOMO-1 orbital is formed through interaction between d orbitals of Ni and the π* antibonding orbitals of CO, forming a feedback π bond that strengthens the Ni–CO coordination. The HOMO-3 comprises a nonbonding V-centered d orbital. The HOMO-4 features an admixture of Ni d orbital character with the σ-donor orbitals from CO. Similar bonding features are consistently observed across the full series of $MNi(CO)_n^-$ clusters (M = Sc, Y, Ti, Zr, Hf, V; n = 3–5). These bonding motifs, persistent throughout the series, lead to notable weakening of the C—O bonds. This relationship indicates that the stabilization of these clusters is largely due to localized π-interactions involving the CO ligands and the bimetallic M–Ni core.

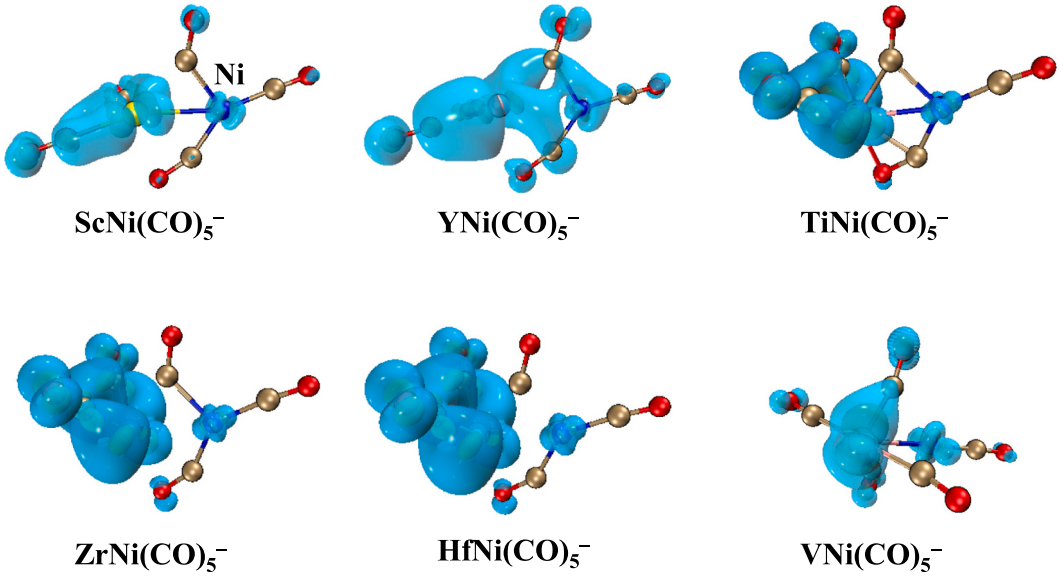

Fig. 17. Isosurface map of unpaired spin density distributions for the most stable isomers of $MNi(CO)_5^-$ (M = Sc, Y, Ti, Zr, Hf, V) (isosurface value = 0.005 a.u.).

4.4.3. Bonding and charge analysis

The distribution of unpaired spin density has been examined for the lowest-energy isomers of the anionic carbonyl complexes $MNi(CO)_n^-$ (M = Sc, Y, Ti, Zr, Hf, *V*; *n* = 3–5) (Fig. 17). While the unpaired electron is mainly on the metal centers, it also delocalizes toward the Ni atom and carbonyl ligands, pointing to substantial M–Ni interaction and significant π-back-donation into the CO π* orbitals. For these the anionic carbonyl complexes, the spin density is strongly concentrated on these early metal atoms. Importantly, the topology of the spin density isosurfaces corresponds well with the predicted asymmetries in the M–Ni–C bonding framework. The pronounced spin delocalization onto the carbonyl ligands highlights considerable metal-to-ligand charge transfer. This transfer directly contributes to weakening the C—O bonds, which is a key step in carbonyl activation and functionalization. These computational visualizations emphasize the key role of the metal in modulating the electronic structure of bimetallic carbonyl complexes. The observed variations in spin density distribution reveal differences in orbital hybridization, bond covalency, and potential catalytic activity across different periods and groups of metals [166,167]. These results elucidate the mechanism for key reactions in these bimetallic systems, such as CO reduction and C—O bond cleavage.

Table 4 summarizes the structural and electronic parameters, including M–Ni Wiberg bond orders, bond lengths, and NPA charges for the series of heterobimetallic carbonyl anions $MNi(CO)_5^-$ (M = Sc, Y, Ti, Zr, Hf, *V*). The M–Ni bond lengths vary considerably across the series, ranging from 2.30 Å in $VNi(CO)_5^-$ to 2.88 Å in $YNi(CO)_5^-$. A clear trend of shorter bond lengths is observed for the early TMs Ti, Zr, Hf, and especially V, indicating stronger bonding in these species. The Wiberg bond orders, which quantify bond multiplicity and strength, are highest for $VNi(CO)_5^-$ (0.44), followed by $HfNi(CO)_5^-$ (0.42) and $ZrNi(CO)_5^-$ (0.41). In contrast, considerably lower values are obtained for $ScNi(CO)_5^-$ (0.32) and $YNi(CO)_5^-$ (0.30), consistent with their elongated bond lengths and indicating comparatively weaker bonding interactions. NPA charges further reveal considerable charge redistribution in these complexes. The nickel center consistently carries negative NPA charges, ranging from −0.18 to −0.49, indicating considerable electron-density accumulation. In contrast, the heterometal M exhibits substantial variation across the series: V attains a strongly negative charge (−0.98), whereas Y bears a positive charge (+0.58). This pronounced variation highlights major differences in the electronic structures and ionicity of the M–Ni bonds, which likely influence the chemical behavior, thermodynamic stability, and reactivity of these bimetallic species. Overall, the data show that boding motifs of the M–Ni strongly depend on the identity of the ancillary metal M. V stands out as particularly distinctive, forming the shortest bond, having the highest bond order, and participating in extensive charge transfer.

5. Conclusion and perspective

5.1. Conclusion

This review provides a systematic investigation of homometallic and heterobimetallic carbonyl complexes using an integrated approach that combines IR–VUV spectroscopy, photoelectron spectroscopy, and quantum chemical calculations. This multifaceted methodology enables a thorough elucidation of structural geometries, electronic properties, and reactivity patterns of well-defined metal species. The coordinated use of experimental and theoretical tools facilitates robust structural identification and the development of coherent bonding descriptions, particularly for transient species that are difficult to isolate or characterize under conventional condensed-phase conditions.

The highly-coordinated $Sc(CO)_7$, $Y(CO)_8$, and $La(CO)_8$ complexes exhibit systematic changes in vibrational properties that correspond to variations in π-back-donation strength among group 3 metals. The observed red-shifts in CO stretching frequencies decrease in the order Sc > Y > La, owing to a progressive reduction in metal d–CO π* orbital overlap down the group. Energy decomposition analysis indicates that covalent orbital interactions primarily stabilize these complexes, with back-donation contributions diminishing as the metal radius increases. The thermodynamic instability of $Sc(CO)_8$, contrasted with the robust stability of $Y(CO)_8$ and $La(CO)_8$, verifies its experimental absence and highlights the critical balance between kinetic accessibility and thermodynamic stability in the gas-phase carbonyl chemistry.

Investigations of neutral titanium carbonyls via IR–*V*UV spectroscopy, which revealed that OTiCCO-based isomers are the predominant species under the experimental conditions, despite predictions that homoleptic $Ti(CO)_n$ complexes are more thermodynamically stable at higher *n*. High-level quantum chemical calculations confirm that the reaction Ti + 2CO → OTiCCO is highly exothermic and proceeds readily, rationalizing the preference for OTiCCO formation in the gas phase. Bonding analysis shows that OTiCCO consists of a cooperative interaction between TiO^+ and CCO^- fragments, stabilized by delocalized π bonding. This system exemplifies how subtle orbital interactions dictate the emergence of unconventional bonding structures in transient molecular species.

For the $MFe(CO)_4^-$ anions (M = Ti, *V*, Cr, Si, Ge, Sn), a clear structural dichotomy emerges. Early TMs (Ti—Cr) favor C_{3v} symmetric trigonal bipyramidal geometries, while group 14 elements (Si, Ge, and Sn) adopt C_{2v} symmetric structures. These geometries are strongly confirmed by the excellent match between experimental VDEs and theoretical predictions. Bonding and charge analyses indicate that the $MFe(CO)_4^-$ (M = Ti, V, Cr) species are best described as M^+ interacting with $[Fe(CO)_4]^{2-}$ fragments, whereas the $MFe(CO)_4^-$ (M = Si, Ge, Sn) species are more accurately represented as neutral M atoms coupled with $[Fe(CO)_4]^-$ units, benefiting from a closed-shell 18-electron Fe center. The observed vibrational red shifts and C—O bond elongations across the series provide detailed molecular-level insight into CO activation mechanisms, analogous to effects seen in surface-bound CO chemistry.

Finally, the $MNi(CO)_n^-$ clusters (M = Sc, Y, Ti, Zr, Hf, V; *n* = 3–5), PES spectra combined with DFT reveal the coexistence of three different CO ligation, making these among the smallest carbonyl systems to incorporate all major coordination modes. A systematic increase in VDEs with cluster size indicates enhanced electronic stabilization from successive CO coordination, reflecting stronger metal–ligand interactions and greater charge delocalization. Orbital and spin density analyses show that the ancillary metal makes a great contribution to regulate Ni–CO back-donation, effectively modulating CO activation. Notably, V-doped metal carbonyls exhibit considerable metal–metal bonding and pronounced charge redistribution, underscoring their potential as molecular mimics of bimetallic active sites in catalytic CO reduction.

Table 4
M − Ni bond lengths, Wiberg bond orders and natural charges of $MNi(CO)_5^-$ (M = Sc, Y, Ti, Zr, Hf, V) species.

Species	M − Ni bond length	M − Ni Wiberg bond order	Natural charge	
			M	Ni
$ScNi(CO)_5^-$	2.73	0.32	0.06	−0.45
$YNi(CO)_5^-$	2.88	0.30	0.58	−0.49
$TiNi(CO)_5^-$	2.58	0.38	−0.35	−0.33
$ZrNi(CO)_5^-$	2.69	0.41	0.11	−0.38
$HfNi(CO)_5^-$	2.66	0.42	0.32	−0.39
$VNi(CO)_5^-$	2.30	0.44	−0.98	−0.18

5.2. Perspective

The findings of this study emphasize the powerful synergy between gas-phase spectroscopy and advanced quantum chemical calculations in revealing bonding patterns and reaction mechanisms in metal carbonyl complexes. With these advances, several unresolved questions and promising research directions deserve further exploration.

First, while this work has focused on early TMs and main-group dopants, the application of similar methodologies to late TMs and polynuclear metal systems could bridge the gap between discrete molecular species and extended catalytic interfaces. In particular, heterobimetallic clusters containing coinage metals or 4d/5d elements may exhibit new bonding regimes and synergistic effects in CO activation that are unattainable in single-metal systems.

Second, while current experimental methods primarily characterize equilibrium structures and thermodynamic properties, real catalytic cycles often involve transient intermediates and dynamic structural changes. The use of time-resolved pump–probe spectroscopy, with femtosecond to picosecond resolution, would enable direct observation of critical processes such as bond cleavage, isomerization, and ligand substitution. These studies could uncover how energy flow and electronic excitation influence reactivity in carbonyl complexes.

Third, although the current theoretical framework depends on DFT and double-hybrid functionals, greater predictive accuracy could be achieved by incorporating multireference wavefunction methods. These advanced approaches better account for near-degeneracies and strongly correlated electronic states, especially in open-shell species such as MFe$(CO)_4^-$ and OTiCCO derivatives. Additionally, machine learning potentials trained on high-level ab initio reference data present a promising strategy to efficiently explore complex potential energy surfaces, enabling faster screening of a wider variety of metal–ligand compositions and structural motifs.

Finally, the present results emphasize the crucial role of understanding CO activation at the molecular level as a model for wider catalytic processes such as CO_2 reduction, Fischer–Tropsch synthesis, syngas conversion, and carbonylation reactions. By systematically examining how metals and ligands influence bond activation, well-define spectroscopic studies provide a fundamental mechanistic framework that supports the rational design of both heterogeneous and homogeneous catalysts. Moreover, combining molecular spectroscopic data with concepts from materials science and nanocatalysis can help bridge gaps between molecular clusters and extended interfacial systems, enabling more accurate prediction and control of catalytic activity and selectivity.

In summary, this work deepens the understanding of bonding in metal carbonyl species and lays a strategic foundation for future studies that combine molecular spectroscopy with applied catalysis. Continuous research in this direction will promote the application of metal carbonyl complexes in sustainable energy conversion, carbon resource valorization, and environmentally friendly synthetic methods, thereby reinforcing the connection between molecular discoveries and practical technological applications.

Declaration of competing interest

The authors declare that they have no known competing financial interests or personal relationships that could have appeared to influence the work reported in this paper.

Acknowledgements

The authors greatly appreciate fruitful callaborations with outstanding colleagues (i.e., Professors Xueming Yang, Jun Li, Mingfei Zhou, Hanshi Hu, Hongjun Fan, etc.) and the contributions of graduate students and postdoctoral fellows. This work was supported by the National Natural Science Foundation of China (NSFC) (22125303, 92361302, 22273101, 22373102, and 21327901), the NSFC Center for Chemical Dynamics (22288201), the Strategic Priority Research Program of the Chinese Academy of Sciences (XDB0970100), the National Key Research and Development Program of China (2021YFA1400501), the Innovation Program for Quantum Science and Technology (2021ZD0303304), the Scientific Instrument Developing Project of the Chinese Academy of Sciences (GJJSTD20220001), the International Partnership Program of the Chinese Academy of Sciences (121421KYSB20170012), the Youth Innovation Promotion Association of the Chinese Academy of Sciences (CAS) (2020187), and Dalian Institute of Chemical Physics (DICP I202437).

Data availability

Data will be made available on request.

References

[1] L. Mond, C. Langer, F. Quincke, L.—Action of carbon monoxide on nickel, J. Chem. Soc. Trans. 57 (1890) 749–753.
[2] L. Mond, F. Quincke, LV.—note on a volatile compound of iron with carbonic oxide, J. Chem. Soc. Trans. 59 (1891) 604–607.
[3] W.E. Trout, The metal carbonyls. I. History; II. Preparation, J. Chem. Educ. 14 (1937) 453.
[4] G. Frenking, N. Frohlich, The nature of the bonding in transition-metal compounds, Chem. Rev. 100 (2000) 717–774.
[5] P. Macchi, A. Sironi, Chemical bonding in transition metal carbonyl clusters: complementary analysis of theoretical and experimental electron densities, Coord. Chem. Rev. 238 (2003) 383–412.
[6] I. Langmuir, The arrangement of electrons in atoms and molecules, J. Am. Chem. Soc. 41 (1919) 868–934.
[7] T.M. Lowry, The electronic theory of valency. Part I. Intramolecular ionisation, Trans. Faraday Soc. 18 (1923) 285–295.
[8] J.S. Wood, Ligand field theory, Nature 226 (1970) 1067–1068.
[9] W. Kutzelnigg, Hans bethe (1906–2005) and ligand field theory, Angew. Chem. Int. Ed. 44 (2005) 3800–3801.
[10] H. Braunschweig, A. Damme, R.D. Dewhurst, A. Vargas, Bond-strengthening π backdonation in a transition-metal π-diborene complex, Nat. Chem. 5 (2013) 115–121.
[11] W. Scherer, V. Herz, A. Brück, C. Hauf, F. Reiner, S. Altmannshofer, D. Leusser, D. Stalke, The nature of β-agostic bonding in late-transition-metal alkyl complexes, Angew. Chem. Int. Ed. 50 (2011) 2845–2849.
[12] G. Bistoni, L. Belpassi, F. Tarantelli, Disentanglement of donation and back-donation effects on experimental observables: a case study of gold–ethyne complexes, Angew. Chem. Int. Ed. 52 (2013) 11599–11602.
[13] D.E. Johnston, M.F. Islam, A.G. Yodh, A.T. Johnson, Electronic devices based on purified carbon nanotubes grown by high-pressure decomposition of carbon monoxide, Nat. Mater. 4 (2005) 589–592.
[14] A. Krapp, G. Frenking, Carbon complexes as electronically and sterically tunable analogues of carbon monoxide in coordination chemistry, J. Am. Chem. Soc. 130 (2008) 16646–16658.
[15] Q.Y. Sun, C. Winstead, V. McKoy, Electronic excitation of carbon monoxide by low-energy electron impact, Phys. Rev. A 46 (1992) 6987–6994.
[16] B.J. Bulkin, C.A. Rundell, Bonding in coordination compounds containing metal-metal bonds, Coord. Chem. Rev. 2 (1967) 371–384.
[17] E. Suljoti, R. Garcia-Diez, S.I. Bokarev, K.M. Lange, R. Schoch, B. Dierker, M. Dantz, K. Yamamoto, N. Engel, K. Atak, O. Kühn, M. Bauer, J.-E. Rubensson, E. F. Aziz, Direct observation of molecular orbital mixing in a solvated organometallic complex, Angew. Chem. Int. Ed. 52 (2013) 9841–9844.
[18] A. Benoit, J.-Y. Le Ma Rouille, C. Mahe, H. Patin, Iron carbonyl complexation of dithioesters. Formation of a chiral carbon center σ-bonded to an iron atom, J. Organomet. Chem. 218 (1981) C67–C70.
[19] C. Lepetit, V. Maraval, Y. Canac, R. Chauvin, On the nature of the dative bond: coordination to metals and beyond. The carbon case, Coord. Chem. Rev. 308 (2016) 59–75.
[20] S.Y. Liu, S.Y. Xia, D.X. Yue, H.R. Sun, H. Hirao, The bonding nature of Fe–CO complexes in heme proteins, Inorg. Chem. 61 (2022) 17494–17504.
[21] W. Liu, Y. Jiang, K.-H. Dostert, C.P. O'Brien, W. Riedel, A. Savara, S. Schauermann, A. Tkatchenko, Catalysis beyond frontier molecular orbitals: selectivity in partial hydrogenation of multi-unsaturated hydrocarbons on metal catalysts, Sci. Adv. 3 (2017) e1700939.
[22] K.D. Nguyen, B.Y. Park, T. Luong, H. Sato, V.J. Garza, M.J. Krische, Metal-catalyzed reductive coupling of olefin-derived nucleophiles: reinventing carbonyl addition, Science 354 (2016) aah5133.
[23] I. Swart, F.M.F. de Groot, B.M. Weckhuysen, D.M. Rayner, G. Meijer, A. Fielicke, The effect of charge on CO binding in rhodium carbonyls: from bridging to terminal CO, J. Am. Chem. Soc. 130 (2008) 2126–2127.
[24] F. Meyer, Y.-M. Chen, P.B. Armentrout, Sequential bond energies of cu$(CO)_x^+$ and ag$(CO)_x^+$ (x = 1-4), J. Am. Chem. Soc. 117 (1995) 4071–4081.
[25] J.M. Weber, The interaction of negative charge with carbon dioxide–insight into solvation, speciation and reductive activation from cluster studies, Int. Rev. Phys. Chem. 33 (2014) 489–519.
[26] G.J. Wang, M.F. Zhou, Infrared spectra, structures and bonding of binuclear transition metal carbonyl cluster ions, Chin. J. Chem. Phys. 31 (2018) 1–11.
[27] H.-J. Freund, G. Meijer, M. Scheffler, R. Schlögl, M. Wolf, CO oxidation as a prototypical reaction for heterogeneous processes, Angew. Chem. Int. Ed. 50 (2011) 10064–10094.
[28] Z.X. Luo, A.W. Castleman Jr., S.N. Khanna, Reactivity of metal clusters, Chem. Rev. 116 (2016) 14456–14492.

[29] M.F. Zhou, L. Andrews, C.W. Bauschlicher, Spectroscopic and theoretical investigations of vibrational frequencies in binary unsaturated transition-metal carbonyl cations, neutrals, and anions, Chem. Rev. 101 (2001) 1931–1962.
[30] Q. Xu, Metal carbonyl cations: generation, characterization and catalytic application, Coord. Chem. Rev. 231 (2002) 83–108.
[31] A.M. Ricks, Z.E. Reed, M.A. Duncan, Infrared spectroscopy of mass-selected metal carbonyl cations, J. Mol. Spectrosc. 266 (2011) 63–74.
[32] N.W. Kinzel, C. Werlé, W. Leitner, Transition metal complexes as catalysts for the electroconversion of CO_2: an organometallic perspective, Angew. Chem. Int. Ed. 60 (2021) 11628–11686.
[33] J. Pazdera, E. Berger, J.A. Lercher, A. Jentys, Conversion of CO_2 to methanol over bifunctional basic-metallic catalysts, Catal. Commun. 159 (2021) 106347.
[34] P.R. Elowe, N.M. West, J.A. Labinger, J.E. Bercaw, Transformations of group 7 carbonyl complexes: possible intermediates in a homogeneous syngas conversion scheme, Organometallics 28 (2009) 6218–6227.
[35] Z. Hendi, R. Pradhan, K. Rachuy, S. Mahmoudi, M.K. Pandey, S.K. Kushvaha, R. Herbst-Irmer, U. Lourderaj, D. Stalke, H.W. Roesky, Phosphasilene mediated CO activation and deoxygenative homo coupling of CO molecules in reactions with metal carbonyls, Chem. Sci. 15 (2024) 18888–18895.
[36] A.E. Sherry, B.B. Wayland, Metalloradical activation of carbon monoxide. Formation and carbonyl coupling of a bent 17 electron M−CO unit, J. Am. Chem. Soc. 111 (1989) 5010–5012.
[37] J.P. Krogman, B.M. Foxman, C.M. Thomas, Activation of CO_2 by a heterobimetallic Zr/CO complex, J. Am. Chem. Soc. 133 (2011) 14582–14585.
[38] H. Schwarz, Metal-mediated activation of carbon dioxide in the gas phase: mechanistic insight derived from a combined experimental/computational approach, Coord. Chem. Rev. 334 (2017) 112–123.
[39] A.J. Poe, D.H. Farrar, Y. Zheng, Systematic kinetics of high nuclearity metal carbonyl clusters. Associative substitution reactions of $Ru_6C(CO)_{17}$ with P-donor nucleophiles, J. Am. Chem. Soc. 114 (1992) 5146–5152.
[40] L. Chen, A.J. Poë, Associative reactions of metal carbonyl clusters: systematic kinetic studies of some ruthenium and other clusters, Coord. Chem. Rev. 143 (1995) 265–295.
[41] C.S.-W. Lau, W.-T. Wong, Synthesis, structural characterisation and electrochemistry of ruthenium carbonyl clusters derived from ferrocenyl (formyl) acetylene, J. Organomet. Chem. 588 (1999) 113–124.
[42] C.E. Juda, R.C. Handford, A.K. Bartholomew, T.M. Powers, N.X. Gu, E. Meyer, N. Roth, Y.-S. Chen, S.-L. Zheng, T.A. Betley, Cluster dynamics of heterometallic trinuclear clusters during ligand substitution, redox chemistry, and group transfer processes, Chem. Sci. 15 (2024) 8242–8248.
[43] T. Bruckhoff, V.J. Kohler, F. Braun, J. Ballmann, L.H. Gade, Dynamics of metal–metal bond dissociation in Pd–Pd and Ni–Ni complexes: reorganization and redistribution reactions of the metalloradicals, Angew. Chem. Int. Ed. 64 (2025) e202514965.
[44] E.G. Mednikov, M.C. Jewell, L.F. Dahl, Nanosized (μ_{12}-Pt) $Pd_{164-x}Pt_x(CO)_{72}(PPh_3)_{20}$ ($x \approx 7$) containing Pt-centered four-shell 165-atom Pd−Pt core with unprecedented intershell bridging carbonyl ligands: comparative analysis of icosahedral shell-growth patterns with geometrically related $Pd_{145}(CO)_x(PEt_3)_{30}$ ($x \approx 60$) containing capped three-shell Pd_{145} core, J. Am. Chem. Soc. 129 (2007) 11619–11630.
[45] J.D. Erickson, E.G. Mednikov, S.A. Ivanov, L.F. Dahl, Isolation and structural characterization of a Mackay 55-metal-atom two-shell icosahedron of pseudo-I_h symmetry, $Pd_{55}L_{12}(\mu_3\text{-}CO)_{20}$ (L = PR_3, R = isopropyl): comparative analysis with interior two-shell icosahedral geometries in capped three-shell Pd_{145}, Pt-centered four-shell Pd–Pt M_{165}, and four-shell Au_{133} nanoclusters, J. Am. Chem. Soc. 138 (2016) 1502–1505.
[46] G. Bussoli, C. Cesari, C. Femoni, M.C. Iapalucci, S. Ruggieri, S. Zacchini, Atomically precise heterometallic rhodium nanoclusters stabilized by carbonyl ligands. In Atomically Precise Nanochemistry, John Wiley & Sons Ltd., Hoboken, NJ, USA, 2023, pp. 309–330.
[47] P.C. Ford, S. Massick, Time resolved spectroscopic studies relevant to reactive intermediates in homogeneous catalysis. The migratory insertion reaction, Coord. Chem. Rev. 226 (2002) 39–49.
[48] K. Miyajima, F. Mafuné, Thermal decomposition of triruthenium dodecacarbonyl investigated by variable-temperature mass spectrometry in the gas phase, Chem. Phys. Lett. 786 (2022) 139191.
[49] G. Bor, U.K. Dietler, P.L. Stanghellini, G. Gervasio, R. Rossetti, G. Sbrignadello, G. A. Battiston, Structural and infrared spectroscopic characterization of $Co_6C(CO)_{12}S_2$: a high-nuclearity carbido carbonyl cluster spontaneously formed from dicobalt octacarbonyl and carbon disulphide, J. Organomet. Chem. 213 (1981) 277–292.
[50] J.J. Venter, M.A. Vannice, A diffuse reflectance FTIR spectroscopic (DRIFTS) investigation of carbon-supported metal carbonyl clusters, J. Am. Chem. Soc. 109 (1987) 6204–6205.
[51] M. Garland, G. Bor, Infrared spectroscopic studies on metal carbonyl compounds. 24. Observation of the infrared spectrum of an acylrhodium tetracarbonyl during the hydroformylation of olefins with rhodium-containing catalyst precursors, Inorg. Chem. 28 (1989) 410–413.
[52] G. Sbrignadello, Calculation of C−O stretching force and interaction constants for the $MCo(CO)_9$ (M = Mn, Tc or re) triad, Inorg. Chim. Acta 48 (1981) 237–242.
[53] S. Clède, F. Lambert, C. Sandt, Z. Gueroui, M. Réfrégiers, M.-A. Plamont, P. Dumas, A. Vessières, C. Policar, A rhenium tris-carbonyl derivative as a single core multimodal probe for imaging (SCoMPI) combining infrared and luminescent properties, Chem. Commun. 48 (2012) 7729–7731.
[54] H. Wang, Y. Xie, R.B. King, H.F. Schaefer, Remarkable aspects of unsaturation in trinuclear metal carbonyl clusters: the triiron species $Fe_3(CO)_n$ ($n = 12, 11, 10, 9$), J. Am. Chem. Soc. 128 (2006) 11376–11384.
[55] C. Policar, J.B. Waern, M.-A. Plamont, S. Clède, C. Mayet, R. Prazeres, J.-M. Ortega, A. Vessières, A. Dazzi, Subcellular IR imaging of a metal–carbonyl moiety using photothermally induced resonance, Angew. Chem. Int. Ed. 50 (2011) 860–864.
[56] B. Rudolf, M. Salmain, J. Grobelny, G. Celichowski, E. Tomaszewska, Synthesis and characterization of metallocarbonyl functionalized gold nanoparticles, Colloids Surf. A Physicochem. Eng. Asp. 385 (2011) 241–248.
[57] M. Salmain, A. Vessières, S. Top, G. Jaouen, I.S. Butler, Analytical potential of near-infrared fourier transform raman spectra in the detection of solid transition metal carbonyl steroid hormones, J. Raman Spectrosc. 26 (1995) 31–38.
[58] F. Yang, P.Y. Yu, J.P. Shi, J. Zhao, X.M. He, J.P. Wang, Two-dimensional infrared spectroscopy of the photoproduct of π-cyclopentadienyliron dicarbonyl dimer, Chin. J. Chem. Phys. 26 (2013) 721–728.
[59] B.J. Aucott, A.-K. Duhme-Klair, B.E. Moulton, I.P. Clark, I.V. Sazanovich, M. Towrie, L.A. Hammarback, I.J.S. Fairlamb, J.M. Lynam, Manganese carbonyl compounds reveal ultrafast metal–solvent interactions, Organometallics 38 (2019) 2391–2401.
[60] V. Singh, Y.J. Zhang, L.P. Yang, P.T. Ma, D.D. Zhang, C. Zhang, L. Yu, J.Y. Niu, J. P. Wang, Two new tetravacant organometallic keggin-type heteropolyoxomolybdates-supported manganese carbonyl derivatives, Molecules 22 (2017) 1351.
[61] M.F. Zhou, L. Andrews, Infrared spectra of CNbO, CMO^-, OMCCO, $(C_2)MO_2$, and $M(CO)_x$ (x = 1-6) (M = Nb, ta) in solid neon, J. Phys. Chem. A 103 (1999) 7785–7794.
[62] M.F. Zhou, L. Andrews, J. Li, B.E. Bursten, Reactions of Th atoms with CO: the first thorium carbonyl complex and an unprecedented bent triplet insertion product, J. Am. Chem. Soc. 121 (1999) 12188–12189.
[63] C.Y. Zhao, R.K. Wu, S.Q. Zhang, X. Hong, Benchmark study of density functional theory methods in geometry optimization of transition metal–dinitrogen complexes, J. Phys. Chem. A 127 (2023) 6791–6803.
[64] A. Diefenbach, F.M. Bickelhaupt, G. Frenking, The nature of the transition metal−carbonyl bond and the question about the valence orbitals of transition metals. A bond-energy decomposition analysis of $TM(CO)_6^q$ ($TM^q = Hf^{2-}$, Ta^-, W, Re^+, Os^{2+}, Ir^{3+}), J. Am. Chem. Soc. 122 (2000) 6449–6458.
[65] J.T. Han, A. Grofe, J.L. Gao, Variational energy decomposition analysis of charge-transfer interactions between metals and ligands in carbonyl complexes, Inorg. Chem. 60 (2021) 14060–14071.
[66] S.G. Patra, C. Paul, N. Dutta, P.K. Chattaraj, Rationalizing the DCD model in transition metal carbonyls: a conceptual density functional theory analysis, J. Comput. Chem. 46 (2025) e70242.
[67] V. Glitz, V.C. Port, E. Nordlander, R.A. Peralta, G.F. Caramori, Choose your level wisely: assessing density functionals and dispersion corrections for metal carbonyl compounds, J. Comput. Chem. 46 (2025) e70245.
[68] G.X. Wang, Decoding the red and blue shift of C−O stretch vibrations in cationic transition metal carbonyl complexes, J. Coord. Chem. 78 (2025) 1645–1658.
[69] J. Pilme, B. Silvi, M.E. Alikhani, Structure and stability of M−CO, M = first-transition-row metal: an application of density functional theory and topological approaches, J. Phys. Chem. A 107 (2003) 4506–4514.
[70] J. Li, G. Schreckenbach, T. Ziegler, A reassessment of the first metal-carbonyl dissociation energy in $M(CO)_4$ (M = Ni, Pd, Pt), $M(CO)_5$ (M = Fe, Ru, Os), and $M(CO)_6$ (M = Cr, Mo, W) by a quasirelativistic density functional method, J. Am. Chem. Soc. 117 (1995) 486–494.
[71] N. Roig, R. Van Lommel, M. Alonso, A.B. Chaplin, Deconvoluting the role of electrostatics in metal carbonyl bonding: dipole moments and energy decomposition analysis of late transition metal pincer complexes, Organometallics 43 (2024) 2787–2796.
[72] M.F. Zhou, L. Andrews, Matrix infrared spectra and density functional calculations of $Ni(CO)_x^-$, x = 1-3, J. Am. Chem. Soc. 120 (1998) 11499–11503.
[73] B. Brehm, M.A. Gusinow, J.L. Hall, Electron affinity of helium via laser photodetachment of its negative ion, Phys. Rev. Lett. 19 (1967) 737–741.
[74] Y. Negishi, H. Kawamata, T. Hayase, M. Gomei, R. Kishi, F. Hayakawa, A. Nakajima, K. Kaya, Photoelectron spectroscopy of germanium-fluorine binary cluster anions: the HOMO-LUMO gap estimation of gen clusters, Chem. Phys. Lett. 269 (1997) 199–207.
[75] A.I. Boldyrev, J. Simons, X. Li, L.-S. Wang, π- and σ-coordinated Al in AlC_2^- and $AlCSi^-$. A combined photoelectron spectroscopy and ab initio study, J. Am. Chem. Soc. 121 (1999) 10193–10197.
[76] X.-B. Wang, J.B. Nicholas, L.-S. Wang, Photoelectron spectroscopy and theoretical calculations of SO_4^- and HSO_4^-: confirmation of high electron affinities of SO_4 and HSO_4, J. Phys. Chem. A 104 (2000) 504–508.
[77] E. Surber, A. Sanov, Photoelectron imaging spectroscopy of molecular and cluster anions: CS_2^- and $OCS^-(H_2O)_{1,2}$, J. Chem. Phys. 116 (2002) 5921–5924.
[78] X.-B. Wang, J.E. Dacres, X. Yang, K.M. Broadus, L. Lis, L.-S. Wang, S.R. Kass, Photodetachment of zwitterions: probing intramolecular coulomb repulsion and attraction in the gas phase using pyridinium dicarboxylate anions, J. Am. Chem. Soc. 125 (2003) 296–304.
[79] X. Yang, X.-B. Wang, E.R. Vorpagel, L.-S. Wang, Direct experimental observation of the low ionization potentials of guanine in free oligonucleotides by using photoelectron spectroscopy, Proc. Natl. Acad. Sci. USA 101 (2004) 17588–17592.
[80] H.-J. Zhai, B. Kiran, B. Dai, J. Li, L.-S. Wang, Unique CO chemisorption properties gold hexamer: $Au_6(CO)_n^-$ (n = 0-3), J. Am. Chem. Soc. 127 (2005) 12098–12106.

[81] H. Xie, Z.B. Qin, X. Wu, Z.C. Tang, L. Jiang, Photoelectron velocity-map imaging signature of structural evolution of silver-doped lead Zintl anions, J. Chem. Phys. 137 (2012) 064318.

[82] Z.B. Qin, R. Cong, X. Wu, Z.L. Liu, H. Xie, Z.C. Tang, L. Jiang, H.J. Fan, Photoelectron velocity-map imaging spectroscopic and theoretical study on the reactivity of the gold atom toward CH_3SH, CH_3OH, and H_2O, J. Chem. Phys. 139 (2013) 034315.

[83] Z.B. Qin, R. Cong, H. Xie, Z.L. Liu, X. Wu, Z.C. Tang, L. Jiang, H.J. Fan, Photoelectron imaging and theoretical study on nascent hydrogen bond network in microsolvated clusters of $au^-(CH_3OH)_n$ (n = 1-5), J. Phys. Chem. A 118 (2014) 3402–3409.

[84] J.H. Zou, H. Xie, D.X. Dai, Z.C. Tang, L. Jiang, Sequential bonding of CO molecules to a titanium dimer: a photoelectron velocity-map imaging spectroscopic and theoretical study of $Ti_2(CO)_n^-$ (n = 1-9), J. Chem. Phys. 145 (2016) 184302.

[85] T. Ebata, A. Fujii, N. Mikami, Vibrational spectroscopy of small-sized hydrogen-bonded clusters and their ions, Int. Rev. Phys. Chem. 17 (1998) 331–361.

[86] B.S. Ault, Matrix isolation infrared spectroscopic and density functional study of the mechanism of the oxidation of CH_3OH by $CrCl_2O_2$, J. Am. Chem. Soc. 120 (1998) 6105–6112.

[87] G.J. Wang, M.F. Zhou, Matrix isolation infrared spectroscopic and theoretical study of the BNNO and AlNNO molecules, Chem. Phys. 342 (2007) 90–94.

[88] Y. Gong, M.F. Zhou, Matrix infrared spectra and density functional calculations of TiO_3 and TiO_5 in solid argon, J. Phys. Chem. A 112 (2008) 9758–9762.

[89] Y. Gong, M.F. Zhou, Infrared spectra of zinc and cadmium dioxide anions in solid neon, Chem. Phys. Lett. 489 (2010) 181–186.

[90] L. Jiang, Q. Xu, Reactions of gold atoms and small clusters with CO: infrared spectroscopic and theoretical characterization of Au_nCO (n = 1-5) and $Au_n(CO)_2$ (n = 1, 2) in solid argon, J. Phys. Chem. A 109 (2005) 1026–1032.

[91] L. Jiang, Q. Xu, Infrared spectra of the $(AgCO)_2$ and Ag_nCO (n = 2-4) molecules in rare-gas matrices, J. Phys. Chem. A 110 (2006) 11488–11493.

[92] Z.-H. Lu, L. Jiang, Q. Xu, Infrared spectra and density functional theory calculations of the tantalum and niobium carbonyl dinitrogen complexes, J. Chem. Phys. 131 (2009) 034512.

[93] D.J. Goebbert, T. Wende, L. Jiang, G. Meijer, A. Sanov, K.R. Asmis, IR spectroscopic characterization of the thermally induced isomerization in carbon disulfide dimer anions, J. Phys. Chem. Lett. 1 (2010) 2465–2469.

[94] Y. Matsuda, M. Mori, M. Hachiya, A. Fujii, N. Mikami, Infrared spectroscopy of size-selected neutral clusters combined with vacuum-ultraviolet-photoionization mass spectrometry, Chem. Phys. Lett. 422 (2006) 378–381.

[95] H.K. Woo, P. Wang, K.C. Lau, X. Xing, C. Chang, C.Y. Ng, State-selected and state-to-state photoionization study of trichloroethene using the two-color infrared-vacuum ultraviolet scheme, J. Chem. Phys. 119 (2003) 9333–9336.

[96] K. Kaizu, M. Kohno, S. Suzuki, H. Shiromaru, T. Moriwaki, Y. Achiba, Neutral carbon cluster distribution upon laser vaporization, J. Chem. Phys. 106 (1997) 9954–9956.

[97] T. Wakabayashi, T. Momose, T. Shida, Mass spectroscopic studies of laser ablated carbon clusters as studied by photoionization with 10.5 eV photons under high vacuum, J. Chem. Phys. 111 (1999) 6260–6263.

[98] Y.J. Shi, S. Consta, A.K. Das, B. Mallik, D. Lacey, R.H. Lipson, A 118 nm vacuum ultraviolet laser/time-of-flight mass spectroscopic study of methanol and ethanol clusters in the vapor phase, J. Chem. Phys. 116 (2002) 6990–6999.

[99] Y. Matsuda, D.N. Shin, E.R. Bernstein, On the zirconium oxide neutral cluster distribution in the gas phase: detection through 118 nm single photon, and 193 and 355 nm multiphoton, ionization, J. Chem. Phys. 120 (2004) 4142–4149.

[100] B.-B. Zhang, X.-T. Kong, S.-K. Jiang, Z. Zhao, H. Xie, C. Hao, D.-X. Dai, X.-M. Yang, L. Jiang, Infrared-vacuum ultraviolet spectroscopic and theoretical study of neutral trimethylamine dimer, Chin. J. Chem. Phys. 30 (2017) 691–695.

[101] B.B. Zhang, X.T. Kong, S.K. Jiang, Z. Zhao, D. Yang, H. Xie, C. Hao, D.X. Dai, X. M. Yang, Z.-F. Liu, L. Jiang, Infrared-vacuum ultraviolet spectroscopic and theoretical study of neutral methylamine dimer, J. Phys. Chem. A 121 (2017) 7176–7182.

[102] B.B. Zhang, Q.-R. Huang, S.K. Jiang, L.-W. Chen, P.-J. Hsu, C. Wang, C. Hao, X. T. Kong, D.X. Dai, X.M. Yang, J.-L. Kuo, L. Jiang, Infrared spectra of neutral dimethylamine clusters: an infrared-vacuum ultraviolet spectroscopic and anharmonic vibrational calculation study, J. Chem. Phys. 150 (2019) 064317.

[103] S. Grimme, J. Antony, S. Ehrlich, H. Krieg, A consistent and accurate ab initio parametrization of density functional dispersion correction (DFT-D) for the 94 elements H-Pu, J. Chem. Phys. 132 (2010) 154104.

[104] S. Grimme, S. Ehrlich, L. Goerigk, Effect of the damping function in dispersion corrected density functional theory, J. Comput. Chem. 32 (2011) 1456–1465.

[105] E. van Lenthe, E.J. Baerends, J.G. Snijders, Relativistic regular two-component Hamiltonians, J. Chem. Phys. 99 (1993) 4597–4610.

[106] E. van Lenthe, E.J. Baerends, J.G. Snijders, Relativistic total energy using regular approximations, J. Chem. Phys. 101 (1994) 9783–9792.

[107] E. van Lenthe, A. Ehlers, E.-J. Baerends, Geometry optimizations in the zero order regular approximation for relativistic effects, J. Chem. Phys. 110 (1999) 8943–8953.

[108] M.P. Mitoraj, A. Michalak, T. Ziegler, A combined charge and energy decomposition ccheme for bond analysis, J. Chem. Theory Comput. 5 (2009) 962–975.

[109] C. Wang, C.-Y. Tian, Y. Zhao, S. Jiang, T.T. Wang, H.J. Zheng, W.H. Yan, G. Li, H. Xie, J. Li, H.-S. Hu, X.M. Yang, L. Jiang, Observation of confinement-free neutral group three transition metal carbonyls $Sc(CO)_7$ and $TM(CO)_8$ (TM = Y, La), Angew. Chem. Int. Ed. 62 (2023) e202305490.

[110] C. Wang, Q.M. Li, X.T. Kong, H.J. Zheng, T.T. Wang, Y. Zhao, G. Li, H. Xie, J. Y. Yang, G.R. Wu, W.Q. Zhang, D.X. Dai, M.F. Zhou, X.M. Yang, L. Jiang, Observation of carbon–carbon coupling reaction in neutral transition-metal carbonyls, J. Phys. Chem. Lett. 12 (2021) 1012–1017.

[111] J.M. Zhang, Z.L. Liu, G. Li, H.J. Fan, L. Jiang, H. Xie, CO activation by the heterobinuclear transition metal-iron clusters: a photoelectron spectroscopic and theoretical study, J. Energy Chem. 63 (2021) 344–350.

[112] B.M. Ju, Z.H. Zhang, X.T. Kong, J.H. Zou, G. Li, H. Xie, L. Jiang, Photoelectron velocity map imaging spectroscopy of group 14 elements and iron tetracarbonyl anionic clusters $MFe(CO)_4^-$ (M = Si, Ge, Sn), J. Chem. Phys. 160 (2024) 044307.

[113] H. Xie, J.H. Zou, Q.Q. Yuan, J.M. Zhang, H.J. Fan, L. Jiang, Photoelectron velocity map imaging spectroscopy of heteronuclear metal–nickel carbonyls MNi(CO)n− (M=Sc, Y; n=2–6), Top. Catal. 61 (2018) 71–80.

[114] J.H. Zou, H. Xie, Q.Q. Yuan, J.M. Zhang, D.X. Dai, H.J. Fan, Z.C. Tang, L. Jiang, Probing the bonding of CO to heteronuclear group 4 metal–nickel clusters by photoelectron spectroscopy, Phys. Chem. Chem. Phys. 19 (2017) 9790–9797.

[115] Q.Q. Yuan, J.M. Zhang, J.H. Zou, H.J. Fan, L. Jiang, H. Xie, Photoelectron velocity map imaging spectroscopic and theoretical study of heteronuclear vanadium-nickel carbonyl anions $VNi(CO)_n^-$ (n = 2-6), J. Chem. Phys. 149 (2018) 144305.

[116] C.X. Chi, H. Qu, L.Y. Meng, F.C. Kong, M.B. Luo, M.F. Zhou, CO oxidation by group 3 metal monoxide cations supported on $[Fe(CO)_4]^{2-}$, Angew. Chem. Int. Ed. 56 (2017) 14096–14101.

[117] C.X. Chi, J.-Q. Wang, H. Qu, W.-L. Li, L.Y. Meng, M.B. Luo, J. Li, M.F. Zhou, Preparation and characterization of uranium–iron triple-bonded $UFe(CO)_3^-$ and $OUFe(CO)_3^-$ complexes, Angew. Chem. Int. Ed. 56 (2017) 6932–6936.

[118] E. Folga, T. Ziegler, A density functional study on the strength of the metal bonds in $Co_2(CO)_8$ and $Mn_2(CO)_{10}$ and the metal-hydrogen and metal-carbon bonds in R-$Mn(CO)_5$ and R-$CO(CO)_4$, J. Am. Chem. Soc. 115 (1993) 5169–5176.

[119] J.-Q. Wang, C.X. Chi, H.-S. Hu, L.Y. Meng, M.B. Luo, J. Li, M.F. Zhou, Triple bonds between iron and heavier group 15 elements in $AFe(CO)_3^-$ (a = as, Sb, bi) complexes, Angew. Chem. Int. Ed. 57 (2018) 542–546.

[120] J.Y. Jin, T. Yang, K. Xin, G.J. Wang, X.Y. Jin, M.F. Zhou, G. Frenking, Octacarbonyl anion complexes of group three transition metals $[TM(CO)_8]^-$ (TM = Sc, Y, La) and the 18-electron rule, Angew. Chem. Int. Ed. 57 (2018) 6236–6241.

[121] J.J. Venter, M.A. Vannice, Carbon-supported $Fe_3(CO)_{12}$, $Ru_3(CO)_{12}$ and $Os_3(CO)_{12}$: decomposition rates, CO adsorption properties and CO hydrogenation behavior, J. Mol. Catal. A-Chem. 56 (1989) 117–132.

[122] C.X. Chi, S. Pan, L.Y. Meng, M.B. Luo, L.L. Zhao, M.F. Zhou, G. Frenking, Alkali metal covalent bonding in nickel carbonyl complexes $ENi(CO)_3^-$, Angew. Chem. Int. Ed. 58 (2019) 1732–1738.

[123] J.Y. Jin, S. Pan, X.Y. Jin, S.J. Lei, L.L. Zhao, G. Frenking, M.F. Zhou, Octacarbonyl anion complexes of the late lanthanides $ln(CO)_8^-$ (ln = tm, Yb, Lu) and the 32-electron rule, Chem. Eur. J. 25 (2019) 3229–3234.

[124] J.-Q. Wang, C.X. Chi, J.-B. Lu, L.Y. Meng, M.B. Luo, H.-S. Hu, M.F. Zhou, J. Li, Triple bonds between iron and heavier group-14 elements in the $AFe(CO)_3^-$ complexes (a = Ge, Sn, and Pb), Chem. Commun. 55 (2019) 5685–5688.

[125] J. Rolke, Y. Zheng, C.E. Brion, S.J. Chakravorty, E.R. Davidson, I.E. McCarthy, Imaging of the HOMO electron density in $Cr(CO)_6$, $Mo(CO)_6$ and $W(CO)_6$ by electron momentum spectroscopy: a comparison with Hartree-Fock and DFT calculations, Chem. Phys. 215 (1997) 191–205.

[126] Z.L. Liu, J.H. Zou, Z.B. Qin, H. Xie, H.J. Fan, Z.C. Tang, Photoelectron velocity map imaging spectroscopy of lead tetracarbonyl-iron anion $PbFe(CO)_4^-$, J. Phys. Chem. A 120 (2016) 3533–3538.

[127] R.D. Ernst, T.J. Marks, J.A. Ibers, Metal-metal bond-cleavage reactions-crystallization and solid-state structural characterization of cadmium tetracarbonyliron, $CdFe(CO)_4$, J. Am. Chem. Soc. 99 (1977) 2090–2098.

[128] R.D. Ernst, T.J. Marks, Chemical and structural relationships among oligomeric compounds $MFe(CO)_4$ (M = Zn, cd, hg), $PbFe(CO)_4$, $AgCo(CO)_4$, and their base adducts, Inorg. Chem. 17 (1978) 1477–1484.

[129] J.M. Zhang, Y. Li, Y. Bai, G. Li, D. Yang, H.J. Zheng, J.H. Zou, X.T. Kong, H.J. Fan, Z.L. Liu, L. Jiang, H. Xie, CO oxidation on the heterodinuclear tantalum–nickel monoxide carbonyl complex anions, Chin. Chem. Lett. 32 (2021) 854–860.

[130] C. Tard, C.J. Pickett, Structural and functional analogues of the active sites of the $[Fe]^-$, $[NiFe]^-$, and $[FeFe]^-$hydrogenases, Chem. Rev. 109 (2009) 2245–2274.

[131] S. Kaur-Ghumaan, M. Stein, [NiFe] hydrogenases: how close do structural and functional mimics approach the active site? Dalton Trans. 43 (2014) 9392–9405.

[132] S. Aguado, M. Gómez-Gallego, L. Casarrubios, M.A. Sierra, Electrocatalytic HER performance of $[FeFe]^-$ hydrogenase mimics bearing M-salen moieties (M = Zn, Ni, Fe, Mn), Chem. Eur. J. 31 (2025) e202403721.

[133] G.H. Kim, J.W. Yang, Research trends in CO_2 utilization: catalytic strategies for sustainable energy and environmental protection, J. CO_2 Util. 101 (2025) 103216.

[134] G. Li, C. Wang, Q.M. Li, H.J. Zheng, T.T. Wang, Y. Yu, M.Z. Su, D. Yang, L. Shi, J. Y. Yang, Z.G. He, H. Xie, H.J. Fan, W.Q. Zhang, D.X. Dai, G.R. Wu, X.M. Yang, L. Jiang, Infrared + vacuum ultraviolet two-color ionization spectroscopy of neutral metal complexes based on a tunable vacuum ultraviolet free-electron laser, Rev. Sci. Instrum. 91 (2020) 034103.

[135] Z.B. Qin, X. Wu, Z.C. Tang, Note: a novel dual-channel time-of-flight mass spectrometer for photoelectron imaging spectroscopy, Rev. Sci. Instrum. 84 (2013) 066108.

[136] W.C. Wiley, I.H. McLaren, Time-of-flight mass spectrometer with improved resolution, Rev. Sci. Instrum. 26 (1955) 1150–1157.

[137] V. Dribinski, A. Ossadtchi, V.A. Mandelshtam, H. Reisler, Reconstruction of Abel-transformable images: the Gaussian basis-set expansion Abel transform method, Rev. Sci. Instrum. 73 (2002) 2634–2642.

[138] M. J. Frisch, G. W. Trucks, H. B. Schlegel, G. E. Scuseria, M. A. Robb, J. R. Cheeseman, G. Scalmani, V. Barone, B. Mennucci, G. A. Petersson, H. Nakatsuji, M. Caricato, X. Li, H. P. Hratchian, A. F. Izmaylov, J. Bloino, G. Zheng, J. L. Sonnenberg, M. Hada, M. Ehara, K. Toyota, R. Fukuda, J. Hasegawa, M. Ishida, T. Nakajima, Y. Honda, O. Kitao, H. Nakai, T. Vreven, J. A. Montgomery Jr., J. E. Peralta, F. Ogliaro, M. J. Bearpark, J. Heyd, E. N. Brothers, K. N. Kudin, V. N. Staroverov, R. Kobayashi, J. Normand, K. Raghavachari, A. P. Rendell, J. C. Burant, S. S. Iyengar, J. Tomasi, M. Cossi, N. Rega, N. J. Millam, M. Klene, J. E. Knox, J. B. Cross, V. Bakken, C. Adamo, J. Jaramillo, R. Gomperts, R. E. Stratmann, O. Yazyev, A. J. Austin, R. Cammi, C. Pomelli, J. W. Ochterski, R. L. Martin, K. Morokuma, V. G. Zakrzewski, G. A. Voth, P. Salvador, J. J. Dannenberg, S. Dapprich, A. D. Daniels, O. Farkas, J. B. Foresman, J. V. Ortiz, J. Cioslowski, D. J. Fox *Gaussian 09*, Revision A.03; Gaussian, Inc.: Wallingford, CT, USA, 2009.
[139] T. Lu, F.W. Chen, Multiwfn: a multifunctional wavefunction analyzer, J. Comput. Chem. 33 (2012) 580–592.
[140] J.P. Foster, F. Weinhold, Natural hybrid orbitals, J. Am. Chem. Soc. 102 (1980) 7211–7218.
[141] A.E. Reed, L.A. Curtiss, F. Weinhold, Intermolecular interactions from a natural bond orbital, donor-acceptor viewpoint, Chem. Rev. 88 (1988) 899–926.
[142] W. Humphrey, A. Dalke, K. Schulten, VMD: Visual molecular dynamics, J. Mol. Graph. 14 (1996) 33–38.
[143] C. Adamo, G.E. Scuseria, V. Barone, Accurate excitation energies from time-dependent density functional theory: assessing the PBE0 model, J. Chem. Phys. 111 (1999) 2889–2899.
[144] ADF 2021.101. https://www.scm.com/, 2026.
[145] E. Van Lenthe, E.J. Baerends, Optimized slater-type basis sets for the elements 1–118, J. Comput. Chem. 24 (2003) 1142–1156.
[146] K.A. Peterson, D. Figgen, E. Goll, H. Stoll, M. Dolg, Systematically convergent basis sets with relativistic pseudopotentials. II. Small-core pseudopotentials and correlation consistent basis sets for the post-d group 16–18 elements, J. Chem. Phys. 119 (2003) 11113–11123.
[147] G.H. Deng, S.J. Lei, S. Pan, J.Y. Jin, G.J. Wang, L.L. Zhao, M.F. Zhou, G. Frenking, Filling a gap: the coordinatively saturated group 4 carbonyl complexes $TM(CO)_8$ (TM = Zr, Hf) and $Ti(CO)_7$, Chem. Eur. J. 26 (2020) 10487–10500.
[148] M.F. Zhou, L. Andrews, Infrared spectra and density functional calculations of small vanadium and titanium carbonyl molecules and anions in solid neon, J. Phys. Chem. A 103 (1999) 5259–5268.
[149] C. Lee, W. Yang, R.G. Parr, Development of the Colle-Salvetti correlation-energy formula into a functional of the electron density, Phys. Rev. B 37 (1988) 785–789.
[150] R. Krishnan, J.S. Binkley, R. Seeger, J.A. Pople, Self-consistent molecular orbital methods. XX. A basis set for correlated wave functions, J. Chem. Phys. 72 (1980) 650–654.
[151] M. Dolg, U. Wedig, H. Stoll, H. Preuss, Energy-adjusted ab initio pseudopotentials for the first row transition elements, J. Chem. Phys. 86 (1987) 866–872.
[152] J. Alessandra Ricca, Charles W. Bauschlicher, Theoretical study of $Fe(CO)_n$, J. Phys. Chem. A 99 (1995) 5922–5926.
[153] M.F. Zhou, L. Andrews, Reactions of laser-ablated iron atoms and cations with carbon monoxide: infrared spectra of FeCO+, Fe(CO)2+, Fe(CO)x, and Fe(CO)x− (x = 1–4) in solid neon, J. Chem. Phys. 111 (1999) 10370–10379.
[154] G.J. Wang, C.X. Chi, J.M. Cui, X.P. Xing, M.F. Zhou, Infrared photodissociation spectroscopy of mononuclear iron carbonyl anions, J. Phys. Chem. A 116 (2012) 2484–2489.
[155] T.H. Dunning Jr., Gaussian basis sets for use in correlated molecular calculations. I. The atoms boron through neon and hydrogen, J. Chem. Phys. 90 (1989) 1007–1023.
[156] D.I. Khomskii, S.V. Streltsov, Orbital effects in solids: basics, recent progress, and opportunities, Chem. Rev. 121 (2021) 2992–3030.
[157] X. Wu, L.L. Zhao, J.Y. Jin, S. Pan, W. Li, X.Y. Jin, G.J. Wang, M.F. Zhou, G. Frenking, Observation of alkaline earth complexes $M(CO)_8$ (M = ca, Sr, or Ba) that mimic transition metals, Science 361 (2018) 912–916.
[158] M. Nakata, T. Shimazaki, PubChemQC project: a large-scale first-principles electronic structure database for data-driven chemistry, J. Chem. Inf. Model. 57 (2017) 1300–1308.
[159] P. Pyykkö, M. Atsumi, Molecular double-bond covalent radii for elements Li–E112, Chem. Eur. J. 15 (2009) 12770–12779.
[160] A.K. Singh, D. Mumbaraddi, V. Mishra, S. Roy, C.P. Vinod, S.C. Peter, Metal deficiency tailored by the 18-electron rule stabilizes metal-based inorganic compounds, Chem. Mater. 35 (2023) 6050–6058.
[161] G. Frenking, Understanding the nature of the bonding in transition metal complexes: from dewar's molecular orbital model to an energy partitioning analysis of the metal–ligand bond, J. Organomet. Chem. 635 (2001) 9–23.
[162] J. Joy, D. Danovich, M. Kaupp, S. Shaik, Covalent vs charge-shift nature of the metal–metal bond in transition metal complexes: a unified understanding, J. Am. Chem. Soc. 142 (2020) 12277–12287.
[163] L. Witteman, M. Lutz, M.-E. Moret, Synthesis of N-heterocycle substituted silyl ligands within the coordination sphere of iron, Organometallics 37 (2018) 3024–3034.
[164] L. Witteman, C.B. van Beek, O.N. van Veenhuizen, M. Lutz, M.-E. Moret, Synthesis and complexation of a free germanide bearing a tridentate N-heterocyclic substituent, Organometallics 38 (2019) 231–239.
[165] A. Jana, V. Huch, H.S. Rzepa, D. Scheschkewitz, A molecular complex with a formally neutral iron germanide motif (Fe_2Ge_2), Organometallics 34 (2015) 2130–2133.
[166] L.L. Qi, J.Q. Guan, Orbital hybridizations in single-atom catalysts for electrocatalysis, Sci. Bull. 70 (2025) 1856–1871.
[167] X.Y. Wang, S.C. Huo, Y.J. Chen, Z. Cai, G.T. Fu, Y. Dai, J.L. Zou, D-orbital hybridization in transition metal electrocatalysts: correlating electronic structure with catalytic performance, Mater. Sci. Eng. R. Rep. 168 (2026) 101147.